SOFT X-RAY SPECTROSCOPY STUDY of WIDE BAND GAP SEMICONDUCTORS-M$_2$PN$_3$ (M=Mg, Zn) and BP$_3$N$_6$

A Thesis Submitted to the

College of Graduate and Postdoctoral Studies

In Partial Fulfillment of the Requirements

For the Degree of Master of Science

In the Department of Electrical and Computer Engineering

University of Saskatchewan

Saskatoon, SK, Canada

By

MD FAHIM AL FATTAH

Permission to Use

In presenting this thesis in partial fulfillment of the requirements for a Postgraduate degree from the University of Saskatchewan, I agree that the libraries of this University may make it freely available for inspection. I further agree that permission for copying of this thesis in any manner, in whole or in part, for scholarly purposes may be granted by the professor or professors who supervised my thesis work or, in their absence, by the Head of the Department or the Dean of the College in which my thesis work was done. It is understood that any copying or publication or use of this thesis or parts thereof for financial gain shall not be allowed without my written permission. It is also understood that due recognition shall be given to me and to the University of Saskatchewan in any scholarly use which may be made of any material in my thesis/dissertation. Requests for permission to copy or to make other use of the material in this thesis in whole or part should be addressed to:

Head of the Department of Electrical and Computer Engineering

57 Campus Drive

University of Saskatchewan

Saskatoon, Saskatchewan S7N 5A9, Canada,

Or

Dean

College of Graduate and Postdoctoral Studies

University of Saskatchewan

116 Thorvaldson Building, 110 Science Place

Saskatoon, Saskatchewan S7N 5C9, Canada.

Part of This Thesis Has Been Published in The Following Article

Abstract

The research on nitridophosphate materials has gained significant attention in recent years due to the abundance of elements like Mg, Zn, P, and N. The compound semiconductors comprising of these earth-abundant elements are important in terms of manufacturing cost of electronic devices and no detrimental impact on the environment. Here in this thesis, a detailed study of band gap and electronic structure of M_2PN_3 (M=Mg, Zn) and BP_3N_6 is presented using synchrotron-based soft X-ray spectroscopy measurements as well as Density Functional Theory (DFT) calculations. The experimental N K-edge X-ray emission spectroscopy (XES) and X-ray absorption spectroscopy (XAS) spectra are used to estimate the band gaps, which are compared with calculations along with the values available in literature. The band gap, which is essential for electronic device applications, is experimentally determined for the first time to be 5.3 ± 0.2 eV, 4.2 ± 0.2 eV, and 5.3 ± 0.2 for Mg_2PN_3, Zn_2PN_3, and BP_3N_6, respectively. The experimental band gaps agree well with the calculated band gaps of 5.4 eV for Mg_2PN_3, 3.9 eV for Zn_2PN_3, and 5.8 eV for BP_3N_6 using the modified Becke-Johnson (mBJ) exchange potential. The states that contribute to the band gap are investigated with the calculated density of states especially with respect to the non-equivalent N sites in the structure. The calculations and the measurements predict that all the three materials studied here in this thesis, have an indirect band gap. The wide band gap of M_2PN_3 (M=Mg, Zn) and BP_3N_6 could make it promising for the application in photovoltaic cells, high power RF applications, as well as power electronic devices.

Acknowledgement

Table of Contents

List of Tables

List of Figures

List of Abbreviations

ALS   Advanced Light Source

CB   Conduction Band

CIGS   Copper Indium Gallium Selenide

CLS   Canadian Light Source

CRT   Cathode Ray Tube

DFT   Density Functional Theory

DOS   Density of States

EXAFS   Extended X-ray Absorption Fine Structure

GE   General Electric

IC   Integrated Circuit

LED   Light Emitting Diode

LINAC   Linear Accelerator

NEXAFS   Near Edge X-ray Absorption Fine Structure

NXES   Non-resonant X-ray Emission Spectroscopy

PDOS   Partial Density of States

PFY   Partial Fluorescence Yield

REIXS   Resonant Elastic and Inelastic X-ray Scattering

RF   Radio Frequency

RXES   Resonant X-ray Emission Spectroscopy

TEY   Total Electron Yield

TFY   Total Fluorescence Yield

UV-Vis	Ultra-Violet Visible Spectroscopy
VB	Valence Band
XAS	X-ray Absorption Spectroscopy
XES	X-ray Emission Spectroscopy

Chapter 1

Introduction

1.1 Motivation

The technological revolution of twentieth century is founded on the groundbreaking evolution of silicon-based transistors, integrated circuits (ICs), light emitting diodes (LEDs), and high-speed electronic devices. But the indirect and comparatively low band gap of silicon has provided the strong motivation for a quest of new materials. According to the Moore's law the number of transistors would be doubled in every two years but the silicon-based technology can not follow the trend indefinitely because of the heating problems caused by packaging in so many transistors in a single chip as well as challenges with leakage current due to shrinking technology. Similarly, it has become a growing challenge to accomplish new power electronic devices with increasing power density and energy efficiency to meet up the market needs using silicon. However, numerous efforts have been made such as 3-D chips and nanotechnology on the computational basis to extend the Moore's law for silicon, but molecular and quantum computing are now in considerations for the post-silicon era.

Currently, high efficiency electronic applications are made with compound semiconductors containing gallium, selenium, cadmium, indium, and tellurium [1]. While CdTe, CIGS (Copper Indium Gallium Selenide) and GaAs were all used for the manufacturing of photovoltaic cells, the solid-state lighting industry was revolutionised by indium-based alloys of GaN and InN [1-3]. In optoelectronics, these nitrides have been very appealing due to the band gap tunability through

alloying. While tremendous success has been accomplished in producing high efficiency lighting technology using III-V nitrides, the price of Indium has substantially increased due to the rapid adoption of Indium Tin Oxide in flat panel display technology [1]. In addition, many of their applications are limited due to the detrimental effect on the environment. Moreover, the reserves in nature of such materials is not sufficient, therefore developing eco-friendly and inexpensive semiconducting materials is of great importance.

Nitridophosphates, a relatively young class of compounds comprised of earth-abundant elements have evolved into one of the best examined classes of nitrides, which have been actively researched in recent years [4]. These compounds are remarkable because various elements can be incorporated thus exhibiting different properties. As nitridophosphate compounds form anionic PN_4 tetrahedra in its structure where electropositive elements can be embedded, they are of great interest, from both scientific point of view as well as for industrial applications [5]. The nitrogen-containing tetrahedral building blocks lead to higher chemical stability in nitridophosphate compounds, higher network charges as well as more covalent bonding which further leading to excellent materials properties [6]. For example, the incorporation of Zn, Mg, B, Ca in the P-N framework in synthesizing Zn_2PN_3, Mg_2PN_3, BP_3N_6, and Ca_2PN_3 have emerged as widely studied materials in recent years [7-11].

Among the above-mentioned compounds, M_2PN_3 (M=Mg, Zn) and BP_3N_6 are studied in this thesis. The metallic nitridophosphate, Mg_2PN_3 and Zn_2PN_3 were synthesized ammonothermally at high pressure and high temperature conditions starting from P_3N_5 and the corresponding metals Mg and Zn [7, 8]. Both materials are colorless as well as transparent, crystallize in a wurtzite type superstructure, which is depicted in Figure 1. Both structures contain two non-equivalent N sites labeled as N1 and N2 in Figure 1.
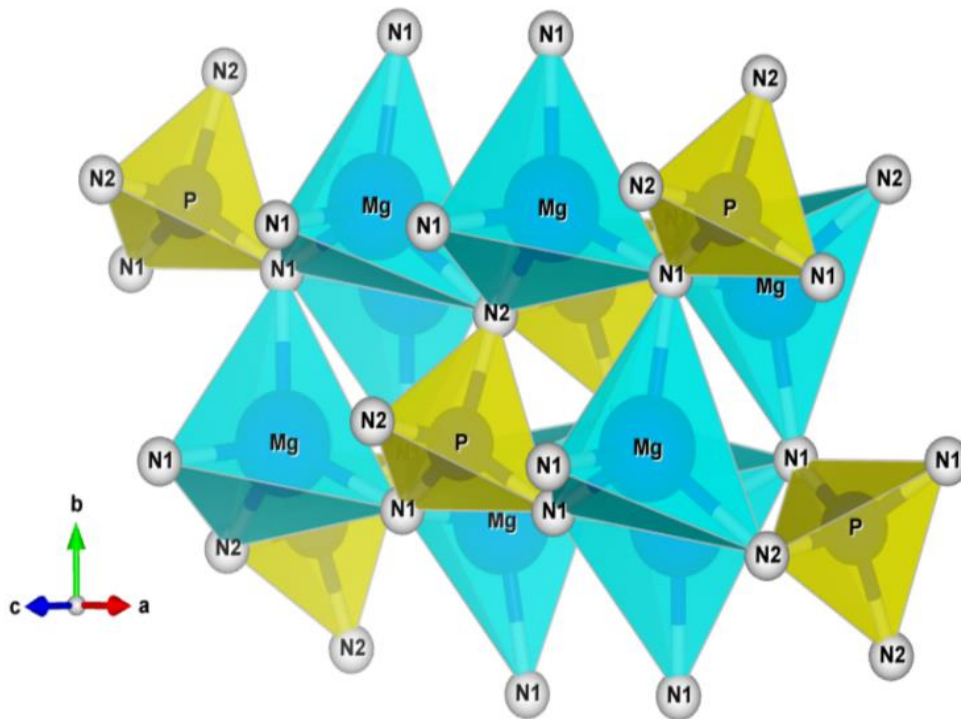
Figure 1.1. Crystal Structure of Mg_2PN_3. MgN_4 and PN_4 tetrahedra are shown in cyan and yellow color, respectively. The two non-equivalent sites of N are labeled as N1 and N2 in white color. The crystal structure of Zn_2PN_3 is essentially the same as that of Mg_2PN_3, only Zn replaces the Mg.

On the other hand, crystals of non-metal nitridophosphate, BP_3N_6 were obtained in an explorative one-step high pressure and high temperature synthesis starting from simple reactive P/N precursor [10]. Owing to its intriguing properties such as high thermal/mechanical stability, photocatalytic activity or chemical inertness, the non-metal nitride, BP_3N_6 has a fundamental interest in solid state chemistry and materials science [6, 10, 12-14]. The crystal structure of BP_3N_6 was determined using X-ray diffraction and depicted in Figure 1.2. This structure contains six non-equivalent N sites indicated as N1 through N6 in Figure 1.2.
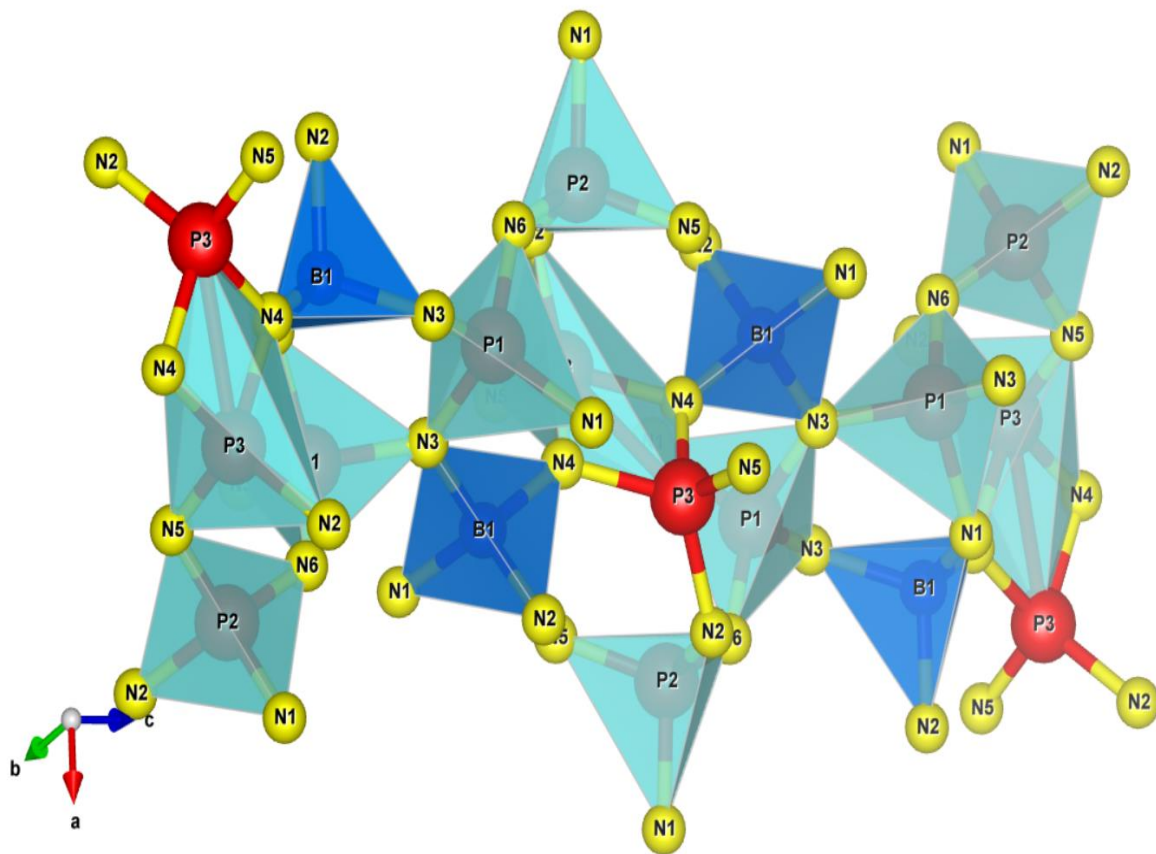
Figure 1.2. Crystal structure of BP_3N_6. Chain-like edge sharing BN_4 and PN_4 tetrahedra are shown in blue and cyan color, respectively. Six non-equivalent N sites (N1 to N6) and three non-equivalent P sites (P1 to P3) are shown in yellow and red color, respectively.

Some nitridophosphates have direct band gaps which are useful for application in light emitting diodes while M_2PN_3 (M=Mg, Zn) and BP_3N_6 exhibit wide, indirect band gaps, which could make them alternative candidates for window materials for tandem thin film photovoltaic cells in the ultraviolet (UV) region to improve quantum efficiency [15-17]. These three wide band gap semiconductors could also be used in UV detectors for defense warning systems, UV communication, space science, environmental monitoring, industrial production, medicine, and

healthcare [18-22]. As the wide band gap material offers higher breakdown voltage, these could be very promising for high power RF as well as power electronic devices. Moreover, the hole effective mass of M_2PN_3 (M=Mg, Zn) and BP_3N_6 is much lower than that of GaN, which is appealing in light of potential applications utilizing p-type conductivity [23].

However, most of the previous work has been devoted to studying the crystal structure, synthesis, and characterizing the optical and thermal behavior of these nitrides. Schnick and co-workers recently reported on the ammonothermal synthesis as well as first investigations of the optical properties of M_2PN_3 (M=Mg, Zn), classifying the compounds as promising semiconductor materials [8, 10]. Using diffuse reflectance UV-Vis spectroscopy and DFT calculations, they reported band gaps of 5 eV and 3.7 eV for Mg_2PN_3 (indirect) and Zn_2PN_3 (direct), respectively. Since the article is centered around the synthesis, their results do not provide information on the density of states (DOS) contribution and the band structure [8]. Therefore, a detailed view inside the electronic structure in emerging high-performance materials like these nitrides is required for the compounds to be optimally employed in a technical application [24]. Until now, no experimental studies have been performed to explore the electronic properties of these nitrides.

This thesis presents the electronic structure of M_2PN_3 (M=Mg, Zn) and BP_3N_6 using X-ray absorption spectroscopy (XAS) and X-ray emission spectroscopy (XES) measurements in conjunction with ab initio density functional theory (DFT) calculations. These techniques directly probe the unoccupied partial density of states (conduction band) and occupied partial density of states (valence band) and offer a complementary measurement of the band gap. This work sets a foundation for a better realization of these compounds in device applications.

This thesis is organized as follows. The fundamental operating principles of synchrotron sources and the generation of synchrotron light is presented in chapter 2. A short description of the two beamlines used in this research is also given. The theory after the X-ray interactions with matter is illustrated in Chapter 3 and describes each spectroscopic technique performed in this work. Chapter 4 outlines the preparation of the samples studied here in and provides a basic overview of experimental as well as theoretical data collection. Results and discussion are presented in Chapter 5. The details analysis of the measured and simulated spectra along with the electronic structure and density of states contribution are described in this chapter. Finally, in chapter 5, the conclusion section ends with a summary of all findings of this study.

Chapter 2

Experimental Facility: The Synchrotron Source

2.1 X-ray Science and Synchrotron Radiation

X-rays have become a powerful tool for the investigation of the nature of materials within the two decades of its discovery by the German scientist, Wilhelm Conrad Röntgen in 1895. Röntgen was awarded with the very first Nobel Prize in Physics in 1901, almost immediately after his discovery to recognize the significance of this work.

The vacuum X-ray tube is the basic source of X-rays in a material and structure analysis laboratory. Only a small fraction of electrons kinetic energy is converted into X-rays on impact upon a metal anode, the majority being lost as heat and a small proportion of the generated X-rays leaves the evacuated apparatus, which is collimated to a narrow beam after removal of unwanted wavelengths by diffraction through a monochromator crystal [25]. The weak diffraction efficiency from the small crystals further makes the whole process extremely inefficient. One solution to the problem is to increase the intensity of the incident X-rays. This can be done by moving the target in its own plane which helps to reduce the heat loading and increase the beam intensity. But the moving anode sources are more expensive than the conventional X-ray tube and the increase in beam intensity is usually less than an order of magnitude, thus the advantages are limited.

Owing to various shortcomings of conventional X-ray sources, physicists began considering alternative sources capable of producing very high intensity X-rays for experimentation. Synchrotron is considered to be such a source of intense and monochromatic X-rays suitable for

studying electronic and physical structure of materials. The synchrotron radiation was first observed by scientists at General Electric (GE) in the United States in 1947 who identified it as a source of energy loss in their 70 MeV synchrotron [26]. There are now more than sixty synchrotron research facilities all over the world dedicated to using the emitted X-ray radiation for the vast range of applications in physics and chemistry to name a few [27]. Synchrotron radiation, a relativistic effect that arises from the fundamental physics with accelerated charged particles travelling on a curved trajectory emit electromagnetic radiation [28]. When the velocity of an electron travelling on a circular path approaches close to the speed of light, the emitted pattern of electromagnetic radiation is folded sharply in forward direction and the power increases substantially. The radiation produced in the synchrotron source is highly collimated and the angular distribution of the beam is in the order of $^1/_\gamma$, where the relativistic γ is defined as the Lorentz factor in terms of the velocity (v) of a particle and the speed of light (c) . The Lorentz factor, γ is given by:

$$\gamma = \frac{1}{\sqrt{1-\frac{v^2}{c^2}}} = \frac{E}{E_0},$$

(2-1)

where v is the electron velocity, c is the speed of light, E_0 (0.511 MeV) is the rest mass of electron, and E is the energy of the storage ring.

The electrons travelling inside the storage ring emit synchrotron light at the instantaneous power per electron, P which is defined by:

$$P[kW] = 8.85 \times 10^{-2} \frac{I[mA]E^4[GeV]}{\rho[m]},$$

(2-2)

where I is the current in the storage ring and ρ is the bending radius. Equation (2-2) clearly shows that the power emitted from the storage ring strongly depends on the energy of the electrons in the beam. This emitted power of radiation can be treated as either a loss mechanism that needs to be overcome in order to replenish the electrons energy or as a precious entity that can be used in experimental endstation. But this high power in the beam is only one of the characteristics of synchrotron radiation; in order to more completely describe the nature of the light and how it can be used in research, it is necessary to examine the structure of synchrotrons more closely [5, 29].
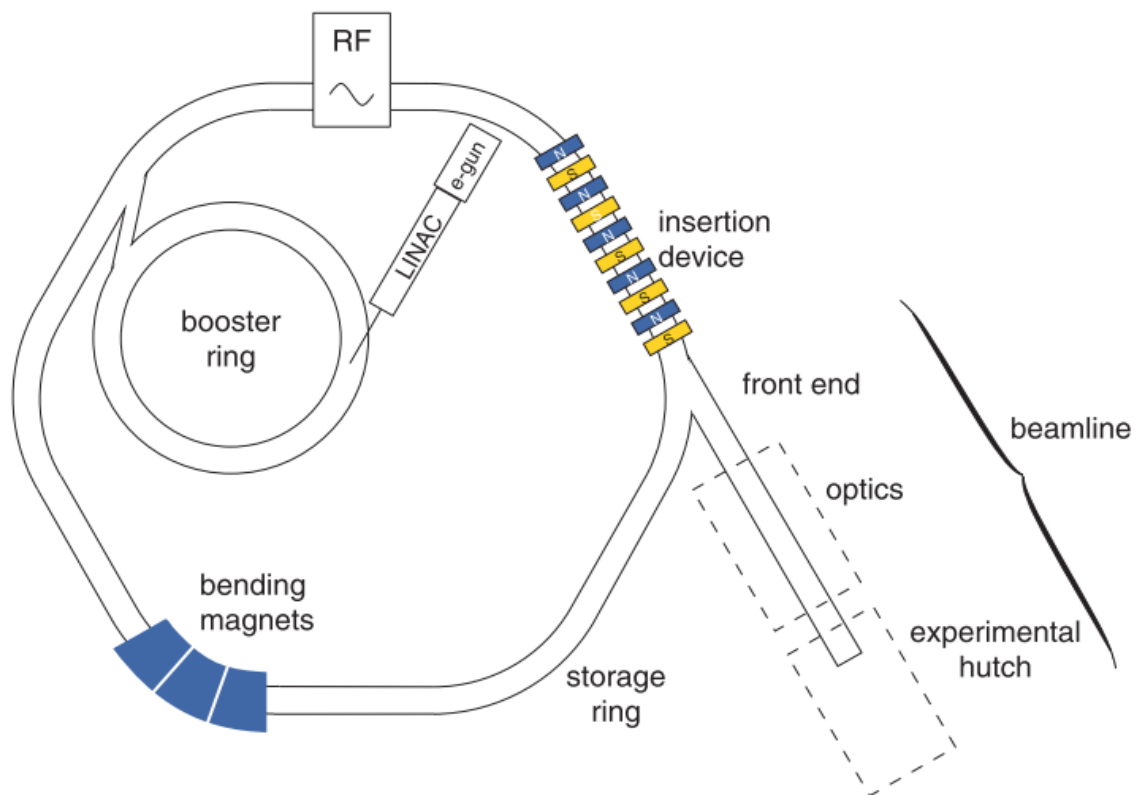
Figure 2.1. A pictorial view of a modern synchrotron source with most essential elements. This figure is reproduced from reference [30].

Two synchrotron facilities, the Canadian Light Source (CLS) at the University of Saskatchewan, Canada and the Advanced Light Source (ALS) at the Lawrence Berkeley National Laboratory, USA were used in this study, both of which are termed as third generation sources designed to emit photons for experimental purposes. The basic design of the above-mentioned synchrotron sources is the same. All the synchrotron radiation sources generally consist of the following basic components: (1) an electron gun and linear accelerator (LINAC), (2) a booster synchrotron, (3) a storage ring, (4) synchrotron radiation beam-lines, and (5) experimental work stations [31]. An example of a modern synchrotron light source with the presentation of its basic elements is shown in Figure 2.1. The following sections briefly describe the key components of a synchrotron source.

2.2 Electron Gun and Linear Accelerator (LINAC)

The primary source of electrons in a synchrotron is provided from an electron gun. The electrons are emitted by thermionic emission. As the high current flows through the cathode, some of the electrons receive enough energy to leave the surface. As this is taking place, a nearby screen is given a short, strong positive charge which pulls the electrons away from the cathode towards the LINAC, a very similar process that of a cathode ray tube [32]. In addition, the high potential difference applied across the cathode also repels the electrons and accelerates them toward the LINAC.

The LINAC consists of a series of Radio Frequency (RF) cavities that accelerate electrons coming from the electron gun to a speed close to that of light. The pulses of electrons produced by the LINAC are injected into the booster ring. At the CLS, for example, the LINAC produces pulses varying from 2 ns up to 140 ns, which are supplied once per second. After several minutes, enough

electrons are accumulated in the storage ring that the synchrotron can operate for several hours and the LINAC can be turned off until more electrons are required to refill the ring [32].

2.3 Booster Ring

The electrons from the LINAC enter into the booster ring where electrons energy are boosted to the operating energy of a facility, for example, 2.9 GeV in case of CLS and 1.9 GeV in case of ALS. The major difference between the LINAC and the booster ring is that the electrons pass through the RF cavity every time they complete the circular path of the booster ring rather than the only once in the LINAC. As a consequence, the circulating electrons in the booster ring receive a boost in energy from RF cavity each time they go around.

At the CLS, as electrons circulate the 103 m booster ring approximately 1.5 million times in 0.6 seconds, they receive a boost in energy from microwave fields generated in the RF Cavity at 2,856 MHz to reach a total energy of 2.9 GeV [32]. On the other hand, at the ALS, the electrons make 1.3 million times revolutions around the booster ring in less than a second to reach their target energy of 1.9 GeV.

Once boosted to full electron energy in the booster ring, electron bunches are periodically injected into the storage ring to maintain the current specified for the storage ring. The injection is generally performed when the current drops by around 70 % of their initial value. The experiments at the beamlines during the injection time are suspended for several minutes referred to as downtime. At the CLS, each injection carries 10 mA of current thus several injections are required to reach the full operating current of storage ring which is 250 mA. Currently CLS is operating on a 12-hour scheduled injection but aiming for the implementation of top-up mode in the near future. In the top-up mode, the booster ring operates at the same energy as the storage ring, but importantly, the

stored current in the ring is quasi-continuously 'topped up' by small injections of electrons, allowing uninterrupted user operation [31]. Typically, the storage-ring current is allowed to drop by approximately 1mA, or less than a percent, before it is topped-up [31]. The ALS regularly operates in a top-up mode where injection occurs every 30-35 seconds to maintain a steady storage ring current [33].

2.4 Storage Ring

When the electrons in the booster synchrotron attain the operating energy, they are transferred by an injection system to the storage ring where they circulate for several hours. The circulation of electrons is maintained by series of magnets namely the dipole or bending magnets, quadrupole magnets and sextupole magnets. The circular storage ring is typically the combination of several arc shaped sections which are connected by some small straight sections. The bending magnets in the arced sections are used to bend the travelling path of electrons causing them to emit photons thus producing synchrotron light. On the other hand, the straight sections are used for the insertion devices like undulators and wigglers to wiggle the electrons back and forth producing a more intense and narrower beam, which is several million times brighter than conventional X-ray sources. The brightest light emitted from the synchrotron is allowed to travel through the round beam ports in the arc sections down to the beamlines. The electrons loose their energy due to the emission of photons, the collision with each other and the remaining particles as the vacuum is not perfect. As a result, the electrons energy must be replenished to maintain the storage ring operating current either by re-injection or by top-up mode.

The CLS storage ring has 171 m of circumference containing twelve arced sections and twelve straight sections. Each arced section has two dipole magnets and a series of quadrupole and

12

sextupole magnets. The straight sections are used to accommodate the insertion devices. The ALS storage ring is 196.8 m in circumference containing the equal curved and straight sections as that of CLS.

2.5 Magnetic Arrangements

The three types of magnets i.e. bending magnets, undulators and wigglers are said to be the heart of a third-generation synchrotron source. These devices attached in the storage ring help producing the photons for experimental use in the beamlines. The characteristics of emitted light from each device are depicted in Figure 2.2 (a), (b), and (c) for bending magnets, wigglers, and undulators respectively. The photon energy vs intensity curve termed as spectral distribution are shown in Figure 2.2 (d), for each device. The detailed characteristics of each device are explained in later this section.

2.5.1 Bending Magnets

A bending magnet is nothing, but a large dipole magnet used to bend the travelling path of electrons thus helping them to travel in the circular trajectory of the storage ring. The fixed strength of magnetic field of the bending magnets emits a fan of X-rays with an angular distribution on the order of $1/\gamma$, as described previously. Though the intensity of radiation is far less than that of insertion devices like wigglers and undulators (Figure 2.2), it still can be used effectively for the less photon-hungry experimental purposes.

Radiation from the bending magnet is emitted in a broad horizontal fan which covers a broad range of energy. The critical energy, E_c is the most important parameter in describing this radiation.
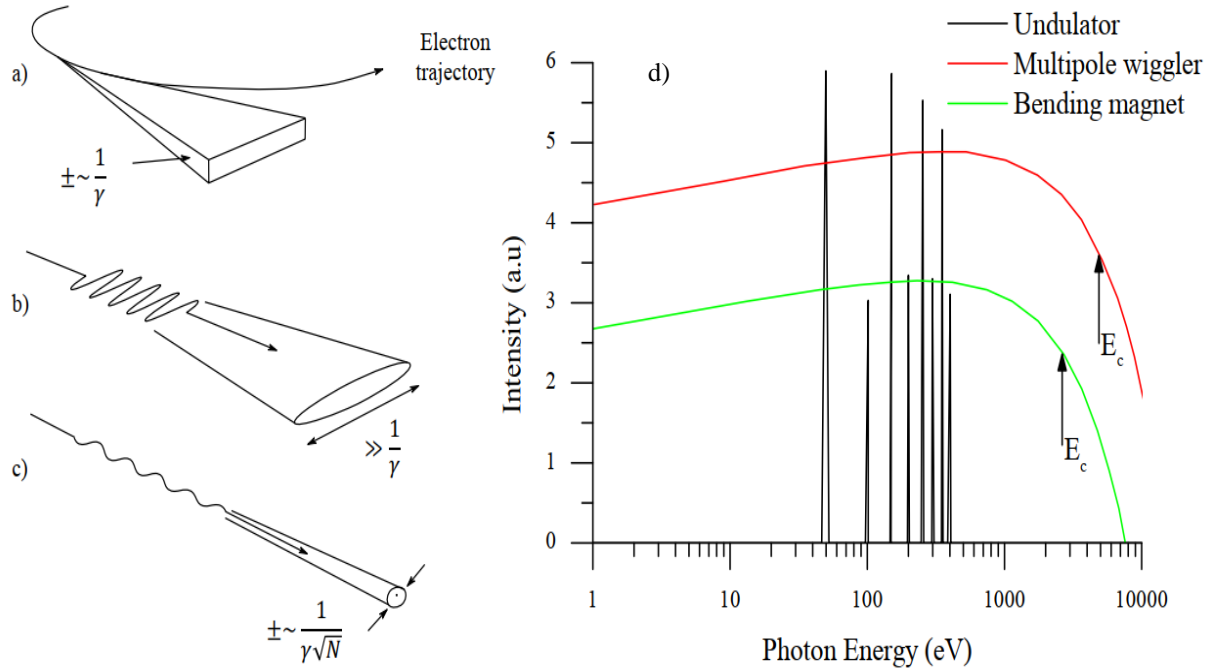
Figure 2.2. A comparison of the emission patterns of light from (a) a bending magnet, (b) a wiggler, and (c) an undulator. (d) A typical spectral distribution. This figure is reproduced from reference [34, 35].

It is defined as the half power point which separates the radiation spectrum into two halves where half the radiated power lies below, and the other half lies above the critical energy. The position of this energy, E_c is given by:

$$E_c(KeV) = \frac{3\hbar c \gamma^3}{\rho} = 0.665 E^2(GeV) B_0(T), \qquad (2\text{-}3)$$

where E is the storage ring energy, B_0 is the strength of the magnetic field, ρ is the radius of the bending magnets, c is the speed of light and γ is the Lorentz factor.

2.5.2 Insertion Devices

As the synchrotron source is used by many users at a time, the radiation requires to be tuned keeping the overall parameters unchanged of the storage ring so that it does not make any impact to other users. Moreover, the radiative power produced by the bending magnet is restricted to the applications in narrower frequency range. These requirements are met by placing insertion devices in the straight sections of storage ring between the bending magnets in the arc segments. Third-generation synchrotrons are characterized using beamline specific insertion devices which can produce considerably higher intensity photons than bending magnets.
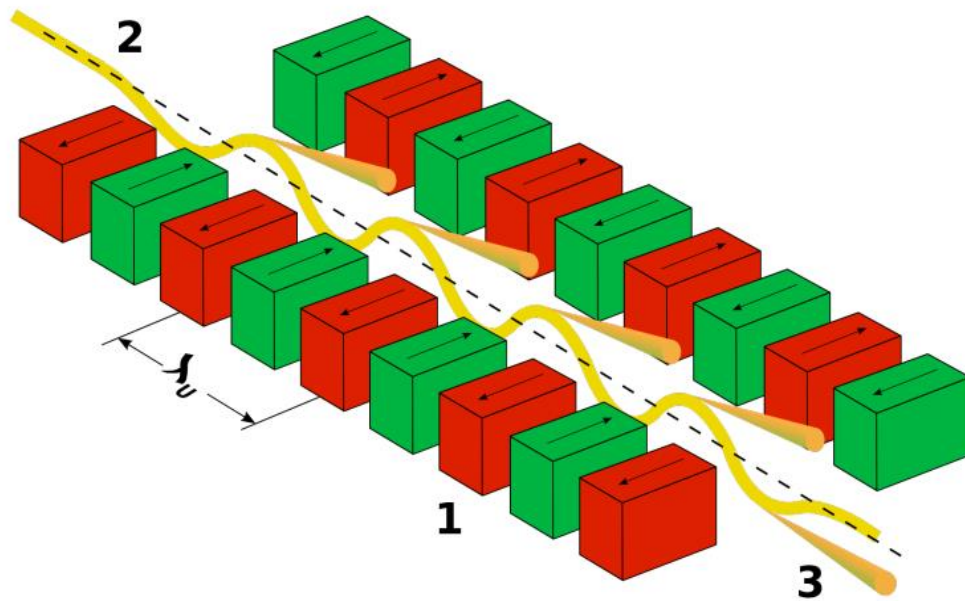
Figure 2.3. Basic design of synchrotron insertion device. This figure is reproduced from reference [36].

There are two general types of insertion devices in a synchrotron source: undulators and wigglers. They are differentiated from each other by the degree to which the electrons are pushed to deflect from a straight path. The insertion devices operate on the force coming from a series of magnets shown in Figure 2.3. The magnets produce sufficient magnetic fields which force the electrons to follow a series of sinusoidal oscillations in the plane of the storage ring generating significantly brighter light than a bending magnet. The geometry of undulators and wigglers can be described with one of the key features, the magnetic deflection parameter K given by [34]:

$$K = \frac{eB}{mc} \frac{\lambda_u}{2\pi}, \tag{2-4}$$

where B is the strength of the magnetic field at the centre of the insertion device and λ_u is the periodicity of the magnetic array [37].

Undulators operate at the unity magnetic deflection, K where the beams of electron receive small magnetic deflection with reference to its initial direction of travel from the magnetic array. Due to the small deflection, the angular width of the radiated beam is also small. As a result, the radiated fields overlap each other, and the constructive interference of certain wavelengths produces a narrow spectral peak as shown in Figure 2.2 (d). The undulator equation [34] can be written as below by considering the necessary conditions for constructive interference along with the electrons trajectory and acceleration while passing through the magnetic array.

$$\lambda_n = \frac{\lambda_u}{2n\gamma^2}\left(1 + \frac{K^2}{2} + \theta^2\gamma^2\right). \tag{2-5}$$

The wavelength λ_n for n^{th} harmonic depends on the storage ring energy (through γ) and undulator

parameters such as periodicity of magnetic array (λ_u) and magnetic deflection parameter (K). θ is the small off axis observation angle.

In an undulator, since the constructive interference of the radiation fields produce semi-monochromatic light, the largest part of the power would be radiated at the fundamental wavelength (n=1) while only a small power can be radiated for odd higher order harmonics (n=3, 5, etc). For low K values, the even harmonics are mostly suppressed which is why they are not important for the experiments. An undulator with N periods can provide N^2 times photon flux than a bending magnet due to the summation of coherent light from every single period. Energy tunability is one of the most important properties of this insertion device. In Equation (2-4), it is possible to adjust the K values by changing the undulator gap which causes the B to be changed. A lower undulator gap will provide higher magnetic fields and vice versa, thus providing the opportunity to tune the energy of the generated light.

On the other hand, wigglers have the same design as the undulators which can be considered as a series of bending magnets but operate with a high value of magnetic deflection parameter (K >> 1). For this K value, the high energy light emitted by each period overlaps between the harmonics producing a much more intense source than the bending magnet. A wiggler with N periods can produce 2N times photon flux than a bending magnet. Moreover, wigglers are suitable to produce much higher energy photons due to the K^2 dependence in Equation (2-5) than undulators, which make them very desirable for hard X-ray beamlines.

2.6 Beamline Description

A beamline consists of a set of instruments which facilitating the use of photons for the experiments. Primary interest for a user in a synchrotron facility is its beamline. A beamline has generally three distinct sections. The first section is an optical hutch with which the photon beam is focused and the wavelengths suitable for the experiments can be selected. The second section is an endstation which consists of a sample holder where the sample is placed for measurements. The last section is a workstation consists of computers which helps the users to control the mechanisms involved with the experiments along with monitor the recorded data.

The beamlines used in this study are the Resonant Elastic and Inelastic X-ray Scattering (REIXS) at the CLS and Beamline 8.0.1 at the ALS have almost similar design as both are used for soft X-ray spectroscopy. Among the many other optical instruments in a beamline only the monochromator will be discussed in the following section.

2.6.1 The Monochromator

While insertion devices like undulators and wigglers can be used to produce brilliant radiation with a low spectral bandwidth, it is crucial for X-ray spectroscopic measurements to use downstream optical instruments to further select for the desired photon wavelength [38]. This job is typically accomplished inside the beamline using a monochromator which is comprised of three interchangeable gratings help users to diffract the desired wavelength for experiment when illuminated by incoming photon. This monochromator also consists of a fixed entrance and a movable exit slit that helps to discard unwanted wavelengths. The layout of the beamline 8.0.1 including the monochromator is shown in Figure 2.4.
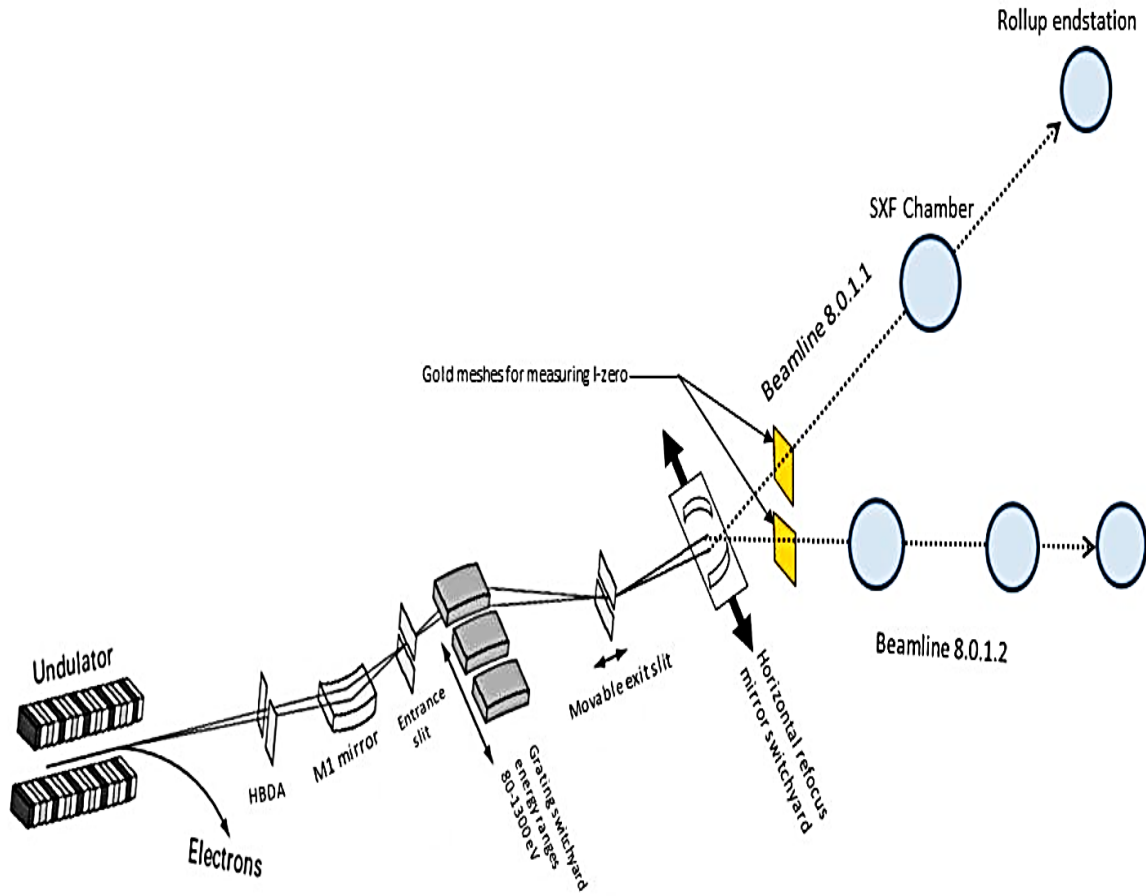
Figure 2.4. Layout of the beamline 8.0.1 at ALS including its main components. This figure is reproduced from reference [39].

Chapter 3

Experimental Techniques

3.1 Basics of Soft X-ray Spectroscopy

X-ray is considered to be a powerful tool for investigating the most important properties of the nano scale materials due to its comparable wavelengths to the radius of an atom. Moreover, the X-ray energies cover the binding energies of atoms, which allow further investigation of the core level electronic structure of a material which accounts for most of the materials properties from color to electrical conductivity to hardness. Soft X-rays (X-rays of energy 50 - 2000 eV) are especially suitable for the study of the elements like carbon, nitrogen, and oxygen, which are important and earth-abundant elements. In this thesis, the soft X-rays are used to study the electronic structure and the density of states of semiconductor materials applying two complimentary techniques such as X-ray Absorption Spectroscopy (XAS) and X-ray emission Spectroscopy (XES). Both the techniques are explained briefly in the subsequent sections.

Before going to address the experimental techniques used herein, the photon-matter interaction needs to be discussed. When an X-ray photon penetrates into matter, it can be absorbed, reflected, refracted, scattered (elastically or inelastically) or transmitted. The soft X-ray spectroscopy involves the excitation of a sample with highly monochromatic photon beam emitted from a synchrotron source and the various resulting effects are monitored using different types of sensors. The first process which is common to all soft X-ray spectroscopic measurements, starts with the excitation of a core electron by absorbing an incident photon. The process is shown schematically

20

in Figure 3.1 and 3.2. When an electron in the ground state (Figure 3.1) of an atom is illuminated with X-ray photons of energy greater than the binding energy of a core level atomic transition, the core electron is promoted leaving a vacant state in the core level. Depending on the incident energy and the structure of the corresponding atom, the excitation can either be resonant or non-resonant. The resonant excitation process referred as photoexcitation shown in Figure 3.2 (a), where one electron from ground state is excited to the previously unoccupied states of the conduction band.
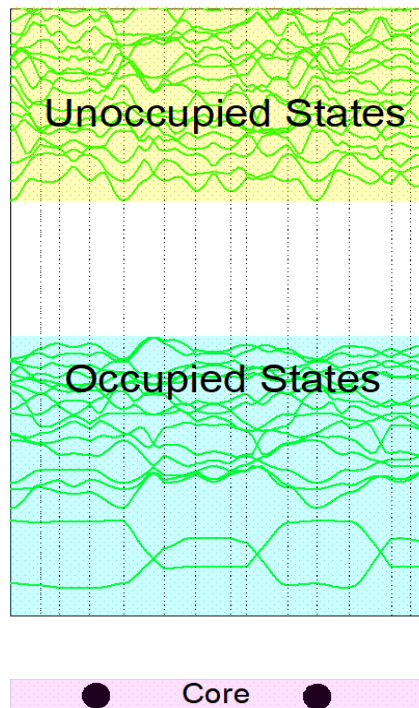
Figure 3.1. Ground state representation of a material.
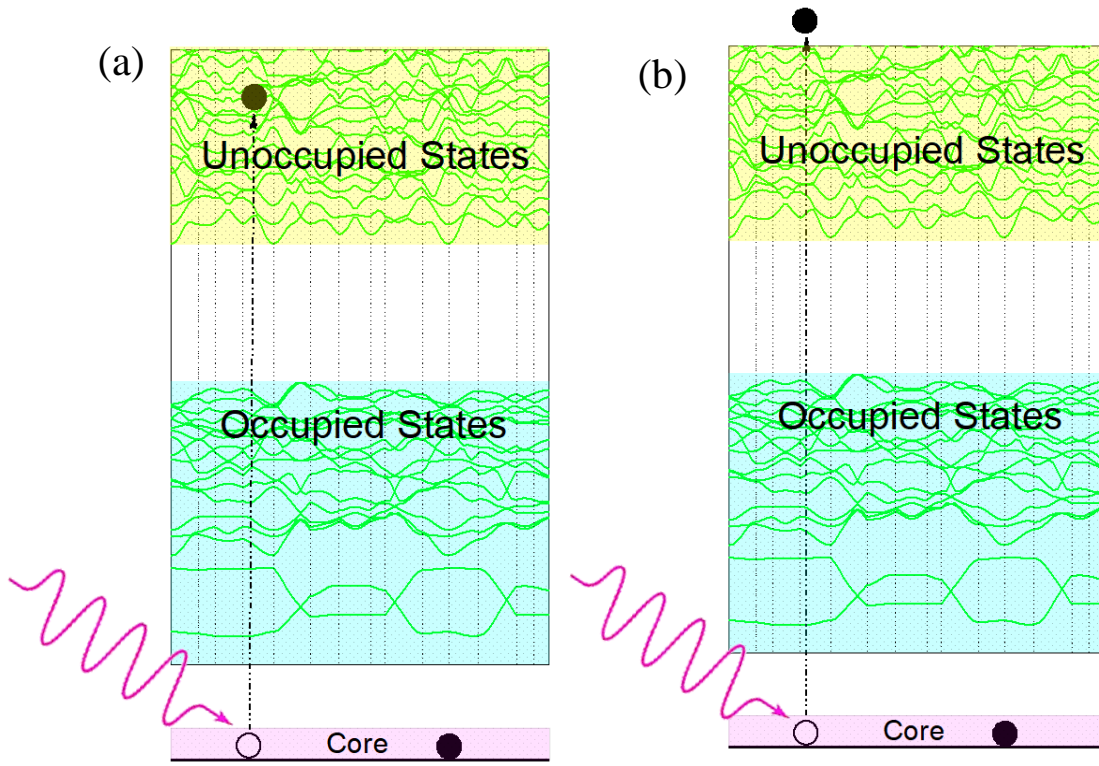
Figure 3.2. Schematic representation of excitation process. An incident X-ray photon excites the core electron into the (a) unoccupied state or (b) completely is removed from the atom.

On the other hand, there is the non-resonant excitation process known as photoionization depicted in Figure 3.2 (b), where the electrons ejected to the continuum and completely leave the atom. After the photon absorption process, the system will rearrange itself by replenishing the created core hole to minimize the total system energy. Following the excitation of core electron, the resulting core hole may be filled by an electron either by radiative (Fluorescence) or non-radiative (Auger) processes. These two processes are illustrated in Figure 3.3. The radiative process in Figure 3.3 (a) where an electron from the occupied states of the valence band decays to fill the core hole by emitting a photon. On the other hand, the non-radiative process in Figure 3.3 (b) occurs when an electron decays down from an excited state to recombine with the core hole by

transferring its energy to a nearby bound electron causing the ejection of that Auger electron instead of releasing the energy by emitting a photon. Among the radiative and non-radiative processes, Auger decay (red curve in Figure 3.4) is more likely for lower atomic number elements, which is shown in Figure 3.4 with dotted blue curve. For elements like carbon (C), Nitrogen (N) and Oxygen (O) having atomic numbers less than 10, below 1% of the core holes created are filled by the radiative process while the non-radiative process contributes more than 99% [37].
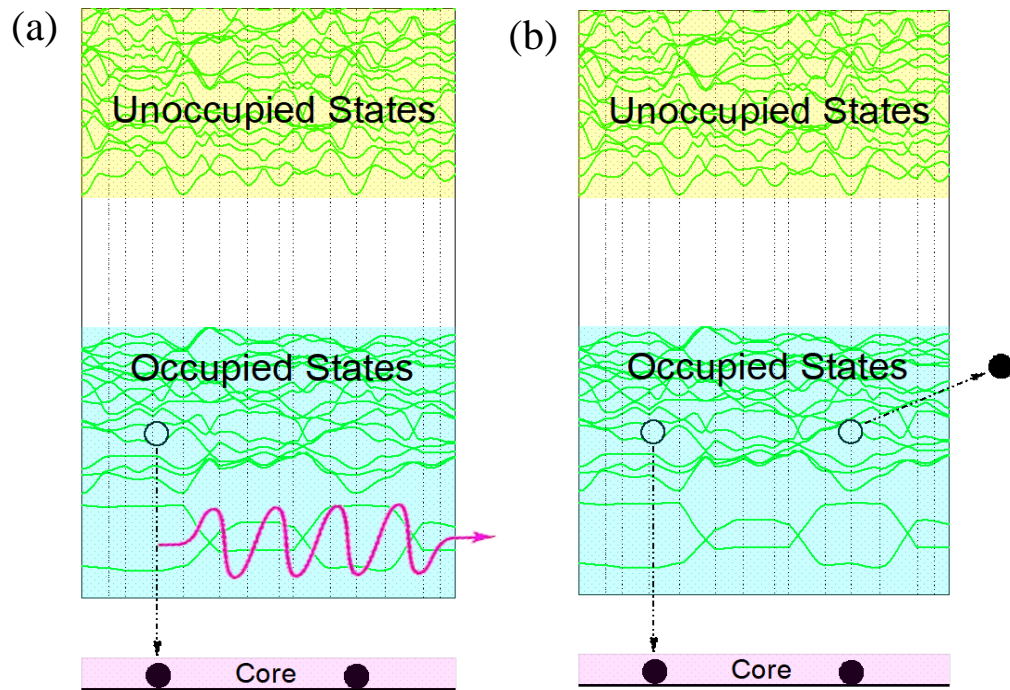
Figure 3.3. Schematic representation of de-excitation process. The created hole in the core can be filled by an electron from an outer shell. The excess energy can either be released in the form of (a) a photon or (b) the ejection of an Auger electron.
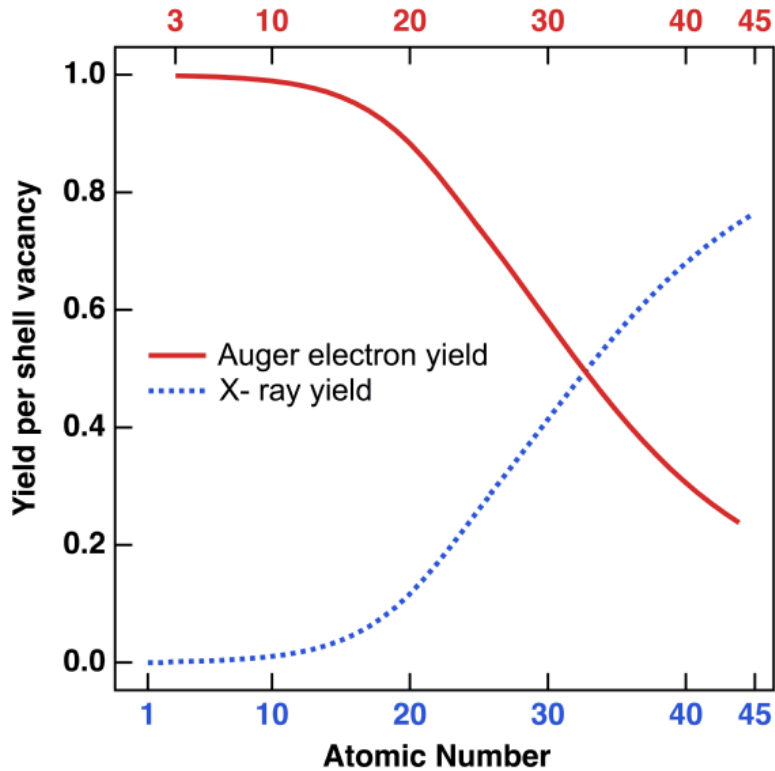
Figure 3.4. Fluorescence yield (dotted blue curve) and Auger electron yields (red curve) as a function of atomic number for K shell vacancies. This figure is reproduced from reference [40].

3.2 Selection Rules

Since not all the radiative transitions from one bound energy state to another are allowed, only those are permitted which follow certain selection rules. The selection rules basically define the change in atomic quantum numbers which are permitted for the excitation and emission process associated with the experimental techniques used herein this thesis. Emission of an X-ray photon in fluorescence must be accompanied by a change in the orbital angular momentum indicated as l by one, that is $\Delta l = \pm 1$ [30]. For instance, since the change in angular momentum is zero, transition

from the 3p level to the 2p level is not allowed. The change in total angular momentum, Δj must be 0 or ± 1 where $j = l \pm s$ for spin $s = 1/2$. However, a transition between two states both with $j = 0$ is not allowed [37]. The change in principle quantum number Δn has no constraint in a radiative phenomenon. The spin does not affect the orbital quantum number and the change in spin quantum is, $\Delta s = 0$. Table 3.1 shows the applicable selection rules for different quantum numbers.

A naming scheme is used in soft X-ray spectroscopy to define a core hole which is refilled creating a spectrum. X-ray absorption spectroscopy uses atomic notation such as 1s to define the core hole while X-ray emission spectroscopy uses letters such as K, L, M, N, …… to define a transition with respect to the principle quantum number $n = 1, 2, 3, 4,$ …… shell. For instance, a transition between 2p to 1s state is denoted by the symbol K_α and a transition between 3p to 1s state is denoted by the symbol K_β, and so on [37]. The Greek letter used in the subscript denotes a particular transition which proceed alphabetically such as α, β, γ and so on. In Figure 3.5, the transitions from $L_{2,3}$ to K and $M_{2,3}$ to K results K_α and K_β lines, respectively. The terminologies of X-ray transition lines are shown in Figure 3.5.

Table 3.1. Summary of dipole selection rules for fluorescence transition.

$\Delta l = \pm 1$
$\Delta j = 0$ or ± 1
$\Delta s = 0$
$\Delta m_j = 0$ or ± 1
Δn has no constraint
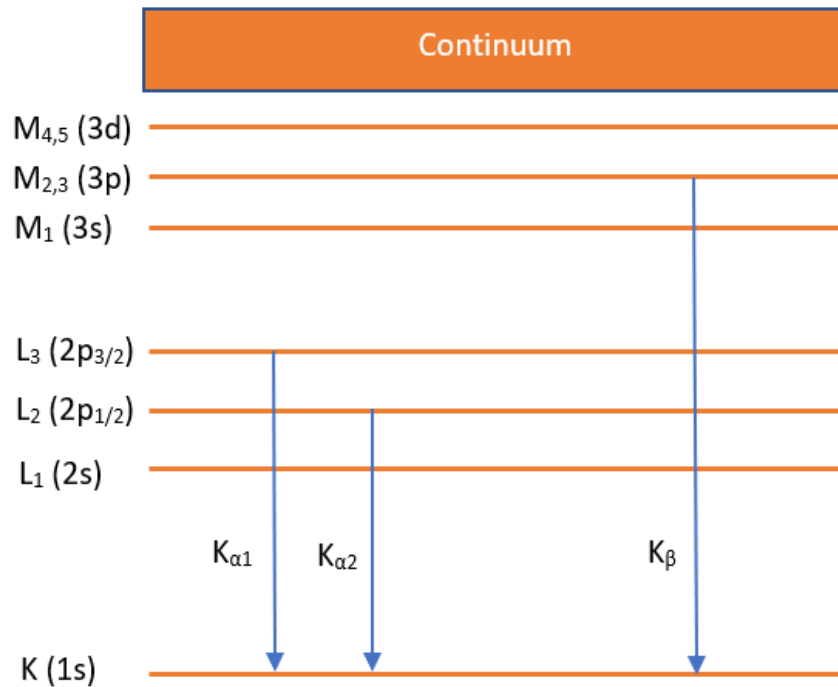
Figure 3.5. A typical electron energy level diagram shows the nomenclature of X-ray transition.

3.3 X-ray Absorption Spectroscopy (XAS)

The X-ray absorption spectroscopy (XAS) was pioneered in the early 20th century, first time used to investigate the materials structure with tunable X-ray sources [41, 42]. Wather Kossel has demonstrated the first example of 3d to 4f transitions in uranium and thorium in his paper which demonstrated the power of XAS to study the atomic structure [43]. From then on, absorption spectra have been a significant tool for the investigation of electronic and chemical properties.
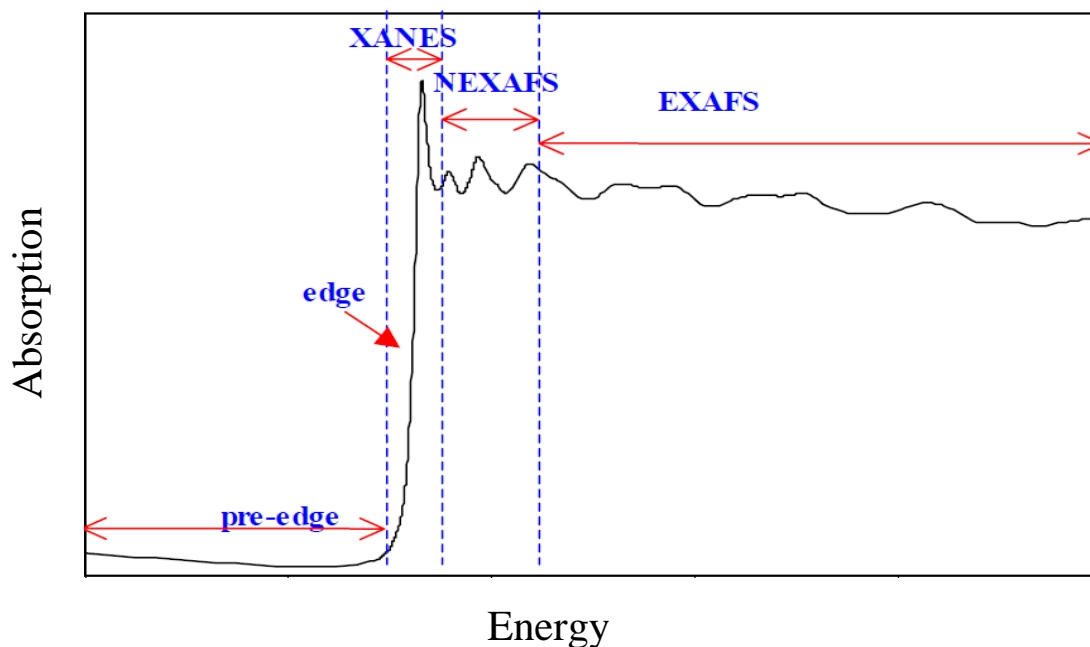
Figure 3.6. A typical XAS spectrum and its different regions. This figure is reproduced from reference [44].

An X-ray absorption spectrum is commonly separated into 4 regions : (i) pre-edge in which the excitation energy is less than the binding energy, (ii) X-ray absorption near edge structure (XANES), where the excitation energy is approximately 10 eV above and below the binding energy, (iii) near edge X-ray absorption fine structure (NEXAFS), is defined as the region between excitation energy of 10 eV up to 50 eV above the edge, and iv) extended X-ray absorption fine structure (EXAFS), which starts approximately from 50 eV and continues up to 1000 eV above the edge [44]. All the four regions are depicted in Figure 3.6. The NEXAFS is a test of the empty partial density of electronic states (PDOS) of a material whereas EXAFS contains the basic structural properties of that material. The measurement of X-ray absorption spectra can be performed at a beamline by scanning the incident energy. At the beginning, the incident energy is not adequate to make an excitation, however when the threshold energy of the core level is reached

27

during the scan, the core electron will get excited to the unoccupied bound states. Eventually, as the excitation energy keeps on increasing, it will be adequate to remove the core electron completely out of the atom which is the reason both the photoexcitation and photoionization features remain in the final absorption spectra. Because of the final state rule, the created core hole may have a major impact on the absorption measurements compared with emission measurements [45]. An excited electron in the unoccupied states of conduction band and a hole formed in the core is referred as the final state for an absorption measurement. The absorption calculation is therefore a direct examination of the unoccupied states in the presence of a transformed core potential. This core hole effect must be taken into consideration while analysing X-ray absorption spectra. On the other hand, in the X-ray emission process, an electron that decays down to fill the core hole from the occupied states, and in most cases its final state is equal to the ground state. Therefore, the core hole in the emission spectrum does not create any major effect.

The precise way to perform the absorption measurement in a sample is to conduct a transmission experiment which involves the intensity measurements of the incident beam of photon before and after the interaction. This method provides a clear indication of how well the photons are absorbed by the sample. There are three different ways to measure XAS, such as (i) total electron yield (TEY), (ii) total fluorescence yield (TFY), and (iii) partial fluorescence yield (PFY), which will be discussed in the next section.

3.3.1 Total Electron Yield (TEY)

The Total Electron Yield (TEY) is the simplest approach for measuring X-ray absorption spectra which depends on measuring the electrons flow from the ground to the sample to replenish the

electrons that removed from the sample. The complete setup for the TEY measurement is shown in Figure 3.7.

As mentioned earlier, the non-radiative process occurs when an electron decays down from an excited state to recombine with the core hole by transferring its energy to a nearby bound electron instead of releasing the energy by emitting a photon. This bound electron, called primary Auger electron leaves the sample and inelastic scattering with Auger electrons leads to a secondary electron cascade [45] which give rise to the total electron yield (TEY) intensity. The secondary electrons with energy greater than the work function can be ejected resulting in a net positive charge on the sample. If the sample is now grounded by connecting a pico ammeter in series, a current will flow to neutralize the sample which is generally assumed to be proportional to the TEY signal.
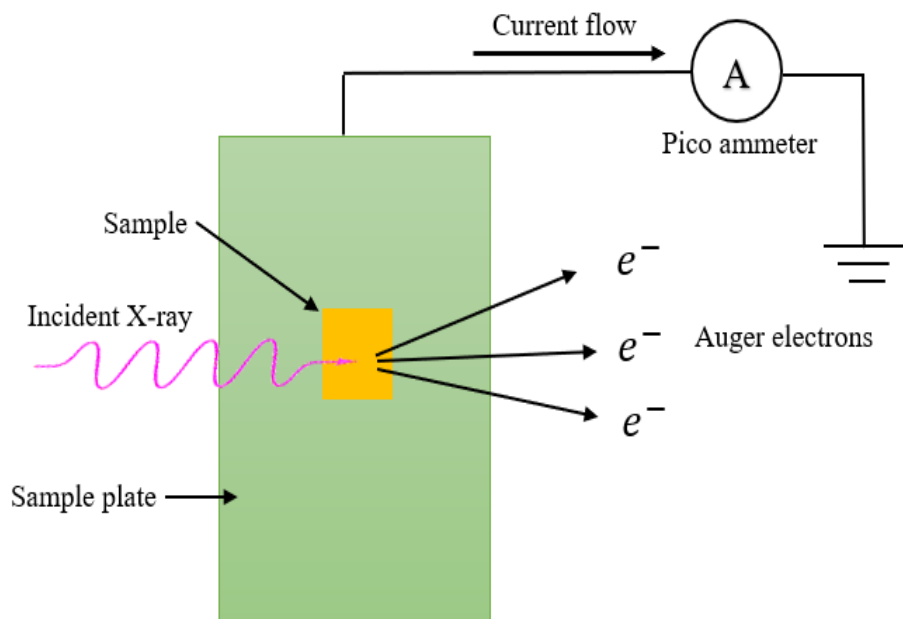
Figure 3.7. Experimental setup for collecting a TEY signal.

The electrons created deeper inside the material lose much energy thus unable to overcome the work function, making this TEY technique a relatively surface sensitive. So if one is involved in researching surface effects or finding surface contaminates, this TEY technique can be helpful. But while working with insulating materials, TEY measurements can be difficult because the materials can build up a charge that will affect the measurement.

3.3.2 Total Fluorescence Yield (TFY)

By using the Total Fluorescence Yield (TFY) method, the problems of TEY technique discussed in the previous section can be solved to some extent though has some shortcomings as well. The TFY technique is the measure of the radiative photons generated during the de-excitation process after the incident X-ray photon is absorbed by the sample differs from the TEY technique which depends on the Auger emission where an electron carries the energy of the excited state. TFY is known to be a bulk sensitive probe compared with surface sensitive TEY technique. The advantage of the TFY technique is that it has a greater escape depth, as photons travel further than electrons. This is due to the mean free path of photon which is on the order of 100 nm at 1000 eV, whereas the electrons escape depth is no more than a few nanometers [41]. Additionally, TFY is the technique of interest where charging of sample is not a significant issue while dealing with highly resistive materials. To measure the TFY signal, a channeltron detector is used to detect the emitted photons irrespective of the photon energy. The detector is mounted in the main chamber close to the measuring sample. When an outgoing photon hits the detector, a free electron will be created and accelerated by a large applied potential. This accelerated electron excites the other electrons along its travel path. The measurement of this cascade of electrons provides the relative absorption of the incoming photons.

3.3.3 Partial Fluorescence Yield (PFY)

The third approach to record a XAS signal is the measurement of partial fluorescence yield (PFY) of a sample. Unlike the TFY technique, here a spectrometer is used as a detector to detect the photons avoiding the need for an additional bias. The spectrometer can be tuned to collect the photons for a certain transition which would provide the additional information of interest. The drawback of this technique is that a significant number of photons are lost since the photons have to pass through an entrance slit and a grating of the spectrometer. By increasing the incident photon flux, the issue of low emitted photon flux can be mitigated somewhat. But it requires longer count times to acquire an acceptable PFY signal.

3.3 X-ray Emission Spectroscopy (XES)

X-ray emission spectroscopy (XES) is said to be the complimentary technique to X-ray absorption spectroscopy (XAS) where the absorption measurements of a material provide the information of the unoccupied density of states (in the conduction band) and the emission measurements provide the picture of partial occupied density of states (in the valence band). The first step of the emission spectrum measurement process is the creation of a core hole by interacting a photon with the sample which is similar to the absorption measurements. But unlike the absorption measurements, here an energy-dispersive detector collects the fluorescent X-ray energies emitted by the decay transitions keeping the incident energy fixed and a wide range of fluorescence energies can be examined [46]. By monitoring the photons with energies corresponding to the decays of electrons from higher occupied states with an energy-dispersive detector, the XES measurement is performed. This decay process results in an occupied core state and a hole in the valance band. According to the final state rule, the density of states in the valence band does not get distorted

since there is no core hole effect. Since the hole in the valence band has negligible effect on the sample, XES offers an accurate measurement of the occupied states.

X-ray emission spectra can be collected in two different ways either in the form of non-resonant X-ray emission spectroscopy (NXES) or in the form of resonant X-ray emission spectroscopy (RXES). Both measurements involve in the promotion of a core electron and the measurement of the radiation during the relaxation process of an electron from higher energy to lower energy state. In non-resonant X-ray emission spectroscopy, the excitation energy of the element of interest is set well above the binding energy of core electron so that it is excited directly to the continuum instead of in the bound unoccupied states. This is in contrast with resonant X-ray emission, where the energy of the incoming photon is such that it excites the core electron to the bound unoccupied states rather than the continuum. RXES spectra are collected after performing an absorption scan in order to determine the energies at which the resonant features are located. Having determined the feature locations, the excitation energy is tuned to record the RXES spectra at a specific resonance.

To record an emission spectrum, a high energy resolution spectrometer is required in order to distinguish the emitted X-ray photons of various energies. In doing so, the high-resolution Rowland-circle spectrometer on Beamline 8.0.1 was used at the Advanced Light Source (ALS) in Berkeley.

Chapter 4

Sample Preparation and Data Collection

4.1 Sample Preparation

The compounds (Mg_2PN_3, Zn_2PN_3 and BP_3N_6) presented in this chapter were prepared by members of Wolfgang Schnick's research group (our collaborator), specifically Mathias Mallmann, Sebastian Vogel and Stefan J. Sedlmaier in the Department of Chemistry at the University of Munich (LMU) in Germany. The following sections outline the preparation and measurement of the samples.

4.1.1 Synthesis of Mg_2PN_3

The first synthesis of Mg_2PN_3 was reported in 1982 by R. Marchand and Y. Laurent in the reference article [47]. They prepared the Mg_2PN_3 from the mixture of Mg_3N_2 and P_3N_5. It crystallizes with orthorhombic symmetry, having space group $Pna2_1$, containing unit cell parameters a = 9.759 (5), b = 5.635 (3), c= 4.743 (3) Å, Z= 4 [47]. It has been identified as the first example of PN_4 tetrahedra in a normal tetrahedral structure type with ordered Mg and P atoms [47].

In 1997, Wolfgang Schnick and co-workers published an article based on the synthesis of Mg_2PN_3 compound in the reference article [9]. They showed that the structural data published by Marchand et al. was inconsistent which did not allow an acceptable conclusion for the existence of the P-N

substructure. In addition, the space group did not show the clear indication of the space community [9]. For these reasons, a thorough review of the structural data was required. In the article [9], Schnick and co-workers reported the pure representation and structural investigation of Mg_2PN_3 and proposed for the first time a possible structure for Mg_2PN_3 [9]. They have synthesized Mg_2PN_3 by the reaction of the respective metal nitrides with P_3N_5 at 800 ℃. The products have been obtained as fine crystalline powders. The crystal structure of Mg_2PN_3 has been determined on the basis of powder diffraction data with cell parameters a = 972.64(8), b = 564.30(5), c = 473.02(2) Å, Z = 4 [9]. They obtained the space group of Mg_2PN_3 as $Cmc2_1$ which is different than the previous study.

Since the high quality and acceptable sizes are required for the applications of these compounds into semiconductor technologies, it is mandatory to have a suitable method for the synthesis and crystal growth like high quality GaN [48]. But the bulk synthesis is the key challenge of these compounds since it requires extremely high temperature and high pressure. For instance, the bulk synthesis of $ZnSnN_2$ can only be synthesized in microcrystalline form at pressures above 5.5 GPa [49]. The ammonothermal process has become a suitable method which was successfully used to synthesize $ZnSiN_2$, $ZnGeN_2$ as well as other nitrides including nitridophosphates with crystallites in the micrometer range [50-53].

The powdered crystals of Mg_2PN_3 used in this thesis for the XAS and XES measurements along with the calculations, was recently synthesized by Mathias Mallmann et al. Air sensitive Mg_2PN_3 was synthesized under ammonothermal conditions (T = 1070 K, P = 140 MPa) starting from Mg, P_3N_5, and NaN_3 using high-temperature autoclaves. Colorless and transparent micro crystalline powder of Mg_2PN_3 were obtained for the first time [8].

The alkali metal azides (NaN_3, KN_3) decompose during reaction and form in situ the corresponding alkali metal amides ($NaNH_2$, KNH_2), acting as ammonobasic mineralizers. They increase the solubility of the other starting materials in ammonia by the formation of soluble intermediate species [52, 54]. Further details about the synthesis method and the characterization of crystal structure of this material can be found in the reference [8].

4.1.2 Synthesis of Zn_2PN_3

In 1986, it was attempted to synthesise Zn_2PN_3 immediately after the concept of a silicate-analogous compound class of nitridophosphates was invented. Around that time, the classical method was implemented at high temperatures using solid-state reactions starting from binary nitrides but ended up without any success.

Later in 2011 phase-pure zinc catena-polynitridophosphate Zn_2PN_3 was synthesized by Stefan J. Sedlmaier et al. [7]. The most challenging part was the synthesis of this zinc nitridophosphate in the sense of limited thermal stability as well as having low decomposition temperature of one of the starting materials P_3N_5. They have been able to successfully synthesize the colorless microcrystalline powder of Zn_2PN_3 using multi-anvil assembly at high pressure and high temperature conditions [7]. The starting materials used for the purpose of synthesis Zn_2PN_3 were pure zinc, P_3N_5 and the alkali metal azides. The azide route proved to be promising in the synthesis of nitridophosphates because of high purity of azides and their chemical stability in air compared to alkali metals or amides. The chemical reactions in preparing Zn_2PN_3 are given below:

$$P_3N_5 \rightarrow 3PN + N_2, \tag{4-1}$$

$$P_3N_5 + 2Zn_3N_2 \rightarrow 3Zn_2PN_3. \tag{4-2}$$

Zn_3N_2 was used in the Equation (4-2), needs to be stabilized beside P_3N_5 [7]. The decomposition of Zn_3N_2 as well as P_3N_5 was prevented by applying a high-pressure of 8 GPa and thereby synthesizing the desired Zn_2PN_3 at around 1200 ºC.

In contrast to the previously published synthesis method, recently Mallmann et al. reported the ammonothermal synthesis of Zn_2PN_3 which was conducted at lower temperatures ($T = 800$ K) and pressures ($p = 200$ MPa) starting from Zn, P_3N_5, and KN_3 [8]. However, the lower temperature results in submicron-sized crystallites of the product, because higher temperatures are needed for improved crystal growth. To overcome this issue, higher pressures seem to be required as already demonstrated in the literature [7], which is not feasible with the current autoclave. More details about the synthesis method and the characterization of crystal structure of this material can be found in the reference articles [7, 8]. Details of cell parameters and space group of Mg_2PN_3 and Zn_2PN_3 are listed in Table 4.1.

4.1.3 Synthesis of BP_3N_6

Unlike the metallic nitrides Mg_2PN_3 and Zn_2PN_3, the non-metal nitridophosphate BP_3N_6 has been barely studied. Due to its exciting material properties such as high thermal or mechanical stability, photo-catalytic activity and chemical inertness [6, 55, 56], Vogel et al. investigated on the synthesis approach of BP_3N_6 which they published in the reference article [10]. In that article, they reported the discovery of the BP_3N_6, obtained during explorative investigation of phosphorus nitrides employing reactive P/N precursors [10]. In a crucible of h-BN; $(PNCl_2)_3$, NH_4N_3, and NH_4Cl reacted at high pressure and high temperature conditions thus resulting the desired BP_3N_6. The problem associated with the synthesis of this nitridophosphate was the decomposition of P/N compounds. According to the theory of Le Chatelier, the high temperature helps NH_4N_3 to

dissociate into N_2 and NH_3, creating high partial pressure of N_2, which eventually prevents the decomposition of targeted P/N compounds [10]. In Equation (4-3), $(PNCl_2)_3$ was used for the purpose of forming one of the starting materials P_3N_5 and NH_4N_3 employed as a mineralizer for the growth of BP_3N_6. The equation is given below according to [10] :

$$2(PNCl_2)_3 + 3NH_4N_3 + 2 \text{ h-BN} \rightarrow 2BP_3N_6 + 12HCl + 4N_2. \qquad (4\text{-}3)$$
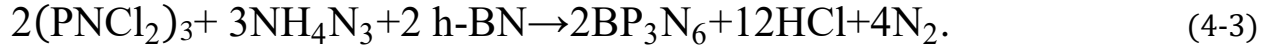
Powdered samples of BP_3N_6 were obtained according to the reaction in Equation (4-3) by the compression of starting materials at 8 GPa heated to 1100 ºC in a multianvil apparatus [10]. The crystal structure of BP_3N_6 was determined using X-ray diffraction method and the acquired data are listed in Table 4.1.

Table 4.1. Crystallographic data of Mg_2PN_3, Zn_2PN_3 and BP_3N_6 obtained from single crystal X-ray diffraction [8, 10].

Formula	Mg_2PN_3	Zn_2PN_3	BP_3N_6
Space group	$Cmc2_1$ (no. 36)	$Cmc2_1$ (no. 36)	$P2_1/c$ (no. 14)
a [Å]	9.50545 (4)	9.4177 (5)	5.0272 (11)
b [Å]	5.64482 (2)	5.4399 (3)	4.5306 (12)
c [Å]	4.70160 (2)	4.9477 (2)	17.332 (3)

4.2 Data Collection

4.2.1 XAS and XES Measurements

Synchrotron-based soft X-ray spectroscopy is a powerful tool to determine the band gap of semiconductors [57]. Third-generation synchrotrons have the capability to produce highly parallel and narrow beams of X-rays with high intensity [58]. Moreover, the energy tunability feature of synchrotrons has made it a unique tool for studying the electronic structure of any material.

The synchrotron-based X-ray absorption and X-ray emission measurements of Mg_2PN_3, Zn_2PN_3 and BP_3N_6 were performed at the Canadian Light Source (CLS) in Saskatoon, Canada as well as at the Advanced Light Source (ALS) in Lawrence Berkeley National Laboratory, USA. The REIXS beamline [59] at CLS was used to record the N 1s edge XAS spectra while the N K_α XES spectra were recorded at 8.0.1 beamline [60] of the Advanced Light Source. The absorption spectra were measured in total fluorescence yield (TFY) mode. The REIXS beamline has a monochromator resolving power (E/ΔE) of about 8000 which translates to an energy resolution of 0.05 eV at an energy of 400 eV for XAS. The resolving power value for the Rowland circle X-ray spectrometer at beamline 8.0.1 is about to 800 which corresponds to an energy resolution (ΔE) of 0.5 eV for XES measurements at an energy of 400 eV.

The powdered sample of Zn_2PN_3 was pressed into indium foil before being placed into the sample transfer chamber, which was initially filled with dry N_2, then evacuated for the measurements [61]. On the other hand, the air and moisture sensitive samples of Mg_2PN_3 and BP_3N_6 were kept inside a glass tube under argon atmosphere after synthesis to prevent surface oxidation. The samples were then mounted under argon atmosphere in a glovebag and loaded into the main chamber for

measurements without exposure to air. Measurements were performed at ultra-high vacuum on the order of 10^{-7} Torr or better than that. All the measured spectra were normalized to the incident photon flux current using a highly transparent gold mesh in front of the sample to measure the intensity fluctuations in the photon beam [62]. Hexagonal boron nitride (h-BN) was used for the purpose of calibrating the energy of the XAS spectrum. The peak at 402.1 eV of h-BN was taken as a reference for calibrating XAS spectrum while the XES spectra were energy calibrated employing the elastic scattering peaks.

4.2.2 Density Functional Theory (DFT) Calculations

A fundamental understanding of materials on an atomic level dimension requires a quantum mechanical description of the solid and thus relies on the calculation of the corresponding electronic structure [63]. Density functional theory (DFT) is a popular approach to perform such calculations, where the many body problem of interacting electrons and nuclei is mapped onto a one electron reference system that in most cases sufficiently models the system [63, 64]. WIEN2k is a commercially available software package employing density functional theory for which experimentally determined crystal structures were used as input to perform different calculations. The crystal structure of Mg_2PN_3 is essentially the same as that of Zn_2PN_3, both have the same space group of $Cmc2_1$ (no. 36) while the BP_3N_6 has a space group of $P2_1/c$ (no. 14). In this thesis, the band structure, DOS, XAS, and XES spectra of M_2PN_3 (M=Mg, Zn) and BP_3N_6 were simulated using the WIEN2k code. While the calculations in WIEN2k using the generalized gradient approximation (PBE-GGA) by Perdew, Burke and Ernzerhof significantly underestimate the band gap, the modified Becke-Johnson (mBJ) exchange potential was used to gain a more appropriate estimation of band gap. The atomic sphere radii for all cases were chosen such that they were

nearly touching, and $R_{MT}^{min}K_{max}$=7 (R is the radius of sphere and K is the reciprocal radius vector) was used for the expansion of basis set [65]. An important feature of this software package is the ability to calculate XAS and XES spectra, which allows for a detailed comparison with experiment. The spectra were calculated by multiplying the relevant atomic and partial density of states with the dipole transition matrix and a radial transition probability [66]. The calculated XAS and XES spectra were broadened using the combination of Lorentzian as well as Gaussian functions to mimic the core hole lifetime broadening and the instrumentation-related broadening, respectively [65]. The calculated XAS spectra are perturbed when a core electron is excited to the unoccupied states leaving a core hole in the valence band. Since the final state in absorption is not a ground state, this perturbation effect is taken into account by removing a core electron from one of the nitrogen atoms in a supercell of $2 \times 2 \times 1$ for M_2PN_3 (M=Mg, Zn) and $2 \times 1 \times 1$ for BP_3N_6 and added as a crystal background charge for overall neutrality.

Chapter 5

Results and Discussion

5.1 Metallic Nitridophosphate, M_2PN_3 (M=Mg, Zn)

5.1.1 N K-edge Spectra of Mg_2PN_3

This section starts with the comparison of experimental XAS and XES spectra with the calculations for Mg_2PN_3. The N Kα XES and N 1s XAS spectra for Mg_2PN_3 are shown in Figure 5.1 alongside with DFT calculated spectra. At first the XAS spectra (top right panel) of Mg_2PN_3 are discussed and then the XES spectra (top left panel) will be discussed.

Excellent agreement is observed between the measured and calculated X-ray absorption spectra. The experimental absorption spectrum was collected in the bulk sensitive total fluorescence yield (TFY) mode shown in Figure 5.1 on the top right panel in red. The main features of the measured XAS spectrum are labeled through I to V and the different colored downward arrows upon the measured XAS spectrum indicate the excitation energies at which the XES spectra (top left panel) were collected.

The calculated XAS spectra for two non-equivalent sites of N atom are also depicted for core hole (CH) calculations. The total calculated spectrum is obtained for core hole (blue) displaying linear combination of individual spectrum of the two non-equivalent N sites (N1 and N2) in Mg_2PN_3. The calculated ground state spectrum is also shown in green color. Comparing the experimental and calculated XAS spectra, it is concluded that the overall agreement with the core hole spectrum

is excellent. All five features labeled I to V of the experimental (TFY) spectrum are reproduced in the calculated core hole spectrum. The intensities of all the features are quite similar. The individual contribution on the features is determined using the calculated core hole spectrum of N1 (pink), N2 (black), and the partial density of states of coordinating atoms (Mg and P).

The p states of all four atoms (Mg, P, N1, and N2) in the crystal structure uniformly contribute to the features I and III (401.6 and 405.6 eV, respectively). According to the calculated core hole spectrum of N1 (pink) and N2 (black), the contribution in features II and IV (404.8 and 410.5 eV, respectively) stem from the p states contribution of N2. The peak at energy 420.4 eV labeled as feature V originates from the d states contribution of Mg.

Having discussed the features of XAS spectra of Mg_2PN_3, the XES spectra in the top left panel of Figure 5.1 are now addressed. Based on the excitation energy, the emission spectra can be divided into two categories. Spectra with excitation energies near the threshold of the conduction band are referred to the resonant X-ray scattering spectra (RXES) where the non-resonant X-ray emission (NXES) spectra are those which are excited at energies well above the conduction band edge.

The calculated non-resonant spectrum (green) of Mg_2PN_3 agrees very well with the measured non-resonant emission spectrum (red). This agreement justifies the crystal structure used for the calculation and the one-electron picture without significant electron correlation. XES spectra in the top left panel of Figure 5.1 were excited both at resonant and non-resonant energies.
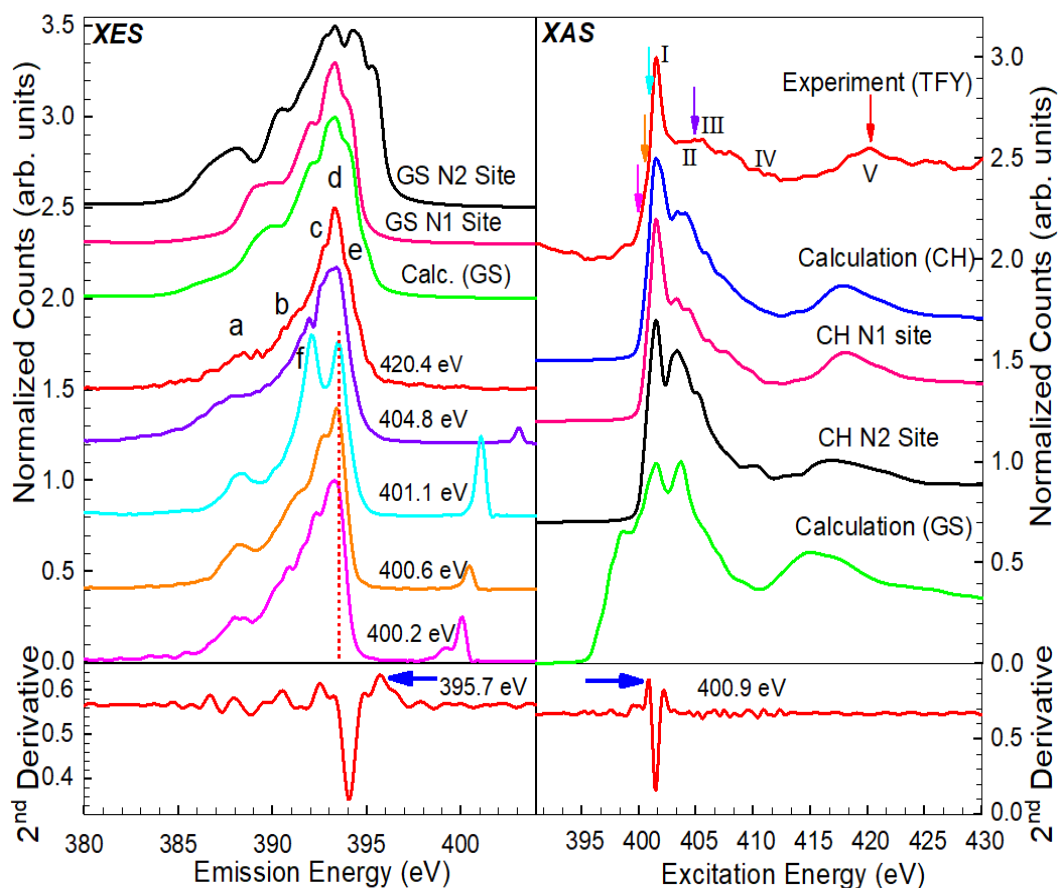
Figure 5.1. (Top left panel) Experimental and calculated N K_α XES spectra of Mg_2PN_3 for different excitation energies. NXES spectrum (red) excited at 420.4 eV and RXES spectra (magenta, orange, cyan, and violet) collected at excitation energies of 400.2, 400.6, 401.1, and 404.8 eV all of which are compared with the ground state (GS, green) calculation. (Top right panel) Experimental TFY (red) is compared with the core hole (CH, blue) and the ground state (GS, green) calculations of N 1s XAS spectra. Separate calculations of the two non-equivalent sites of N (N1 and N2) are shown to understand their individual contributions to both, XES and XAS spectra. Different colored downward arrows on the absorption spectrum indicate the excitation energies for RXES and NXES spectra. (Bottom left and right panel) Second derivative of experimental XES and XAS spectra with the corresponding peaks of valence band and conduction band onsets indicated by blue arrows.

The resonant excitation energies at 400.2 eV (magenta) and 400.6 eV (orange) excited along the conduction band edge results similar emission spectra. But the spectrum excited at 401.1 eV (cyan) is quite interesting because of an additional peak labeled as f. This could be because of several reasons. The two non-equivalent sites of N are one of them and the other reason could be due to excitation near the main peak at II. If this is because of the two non- equivalent sites, then it is obvious to expect this feature in other excitation energies as well. But this feature vanishes at all other energies including the energies near the main peak at II. So, both possibilities are excluded. The spaghetti like bands could be the reason to give rise such a prominent peak like feature f. The resonant excitation energy at 404.8 eV selectively excites the N2 site for which the violet color emission spectrum resembles to some extent the ground state calculation of N2 site (black).

Now these (400.2, 400.6, and 401.1 eV) RXES spectra will be used, which are excited along the conduction band edge to experimentally determine whether the Mg_2PN_3 has a direct or indirect band gap. The RXES process obeys the momentum conservation and momentum transfers are negligible for the soft X-ray photons and our scattering geometry. This confines that only valence band electrons with the same wave vector as the excited electron in the conduction band can fill the core hole. These decay processes lead to the k-conserving part of the RXES spectrum [67, 68]. For direct band gap materials, the RXES spectrum containing the highest emission energy is obtained by the lowest incident photon. On the other hand, for an indirect band gap material, the highest emission energy is obtained for excitation at some higher excitation energy with respect to the lowest incident photon as the k-conservation means that decays from the valence band maximum will not be detected for the lowest incident photon energies. The vertically dotted red line in Figure 5.1 (top left panel) indicates that the highest emission energy is observed for higher excitation energies with respect to the lowest excitation energy. This is a signature of the indirect

band gap of Mg_2PN_3 [67, 68]. On the other hand, the non-resonant emission spectrum excited at 420.4 eV (red) has five features indicated as a to e, all of which are matched very well with the calculated ground state (green) spectrum. Feature a is responsible for the contribution of 2p states of the N2 site while all other features from b to e are contributed from the 2p states of N1 site.

5.1.2 Band Gap Determination of Mg_2PN_3

Now the gap between the valence band (VB) and the conduction band (CB) edge is determined by applying the second derivative on the measured XES and XAS spectra shown in the bottom two panels of Figure 5.1. This method is unambiguous and yields more reproducible band gap values than the conventional linear extrapolation method. Selecting the first maximum (indicated by the blue horizontal arrow) above the noise level in the second derivative curve on the bottom panels of Figure 2, a gap of 5.2 eV between VB and CB edges is obtained. Since the N 1s core hole in the final state of the XAS measurement distorts the unoccupied density of states, this effect needs to be taken into account in determining the corrected band gap. The shift in the calculated core hole is determined from the energy difference between the conduction band onsets of core hole spectrum and the ground state spectrum. For Mg_2PN_3, a 0.1 eV shift is observed resulting in a final experimental band gap of 5.3 ± 0.2 eV. The 0.2 eV uncertainty in energy stems from the energy calibration, the monochromator, and the spectrometer resolution.

This experimental band gap is in excellent agreement with the calculated band gap of 5.4 eV using the mBJ exchange correlation potential but differs from the calculated gap of 3.7 eV using PBE-GGA, which is known to underestimate the band gap [69-71]. The band gap obtained in this study is also in reasonable agreement with prior work [8], which reported a value of 5 eV using diffuse reflectance spectroscopy.

5.1.3 N K-edge Spectra of Zn_2PN_3

Having addressed the band gap and the detailed comparison of measured and calculated spectra of Mg_2PN_3, a similar approach is used to discuss Zn_2PN_3. Figure 5.2 displays the measured XES and XAS spectra of Zn_2PN_3 alongside with simulated spectra. The experimental XAS spectrum (red) on the top right panel of Figure 5.2 agrees quite well with the calculated one. Three key features are indicated as I to III on the measured TFY spectrum, most of them are matched with the calculated core hole (blue) spectrum while having some deviations with ground state (cyan) calculations.

Feature I in the experimental spectrum has almost equal contributions from the p states of the two non-equivalent N sites and P. The small shoulder on the feature II observed in both experiment and core hole spectra, stems from the contribution of p states of N2 site. The contribution in feature III stems from the hybridization of d states of P and p states of N1 atom. Among the three features, two of them are exactly matched between the core hole and the experimental spectra but feature I has better agreement between the experiment and the ground state calculation. A sharp rise in the CB edge is seen in both measured and calculated core hole spectra but the ground state spectrum shows a relatively flat CB edge.

As mentioned earlier, the emission spectra can be divided into two categories, RXES and NXES. The calculated non-resonant spectrum of Zn_2PN_3, agrees well with the measured non-resonant emission spectrum justifying the validity of the crystal structure of Zn_2PN_3, which was used as input for the calculation.
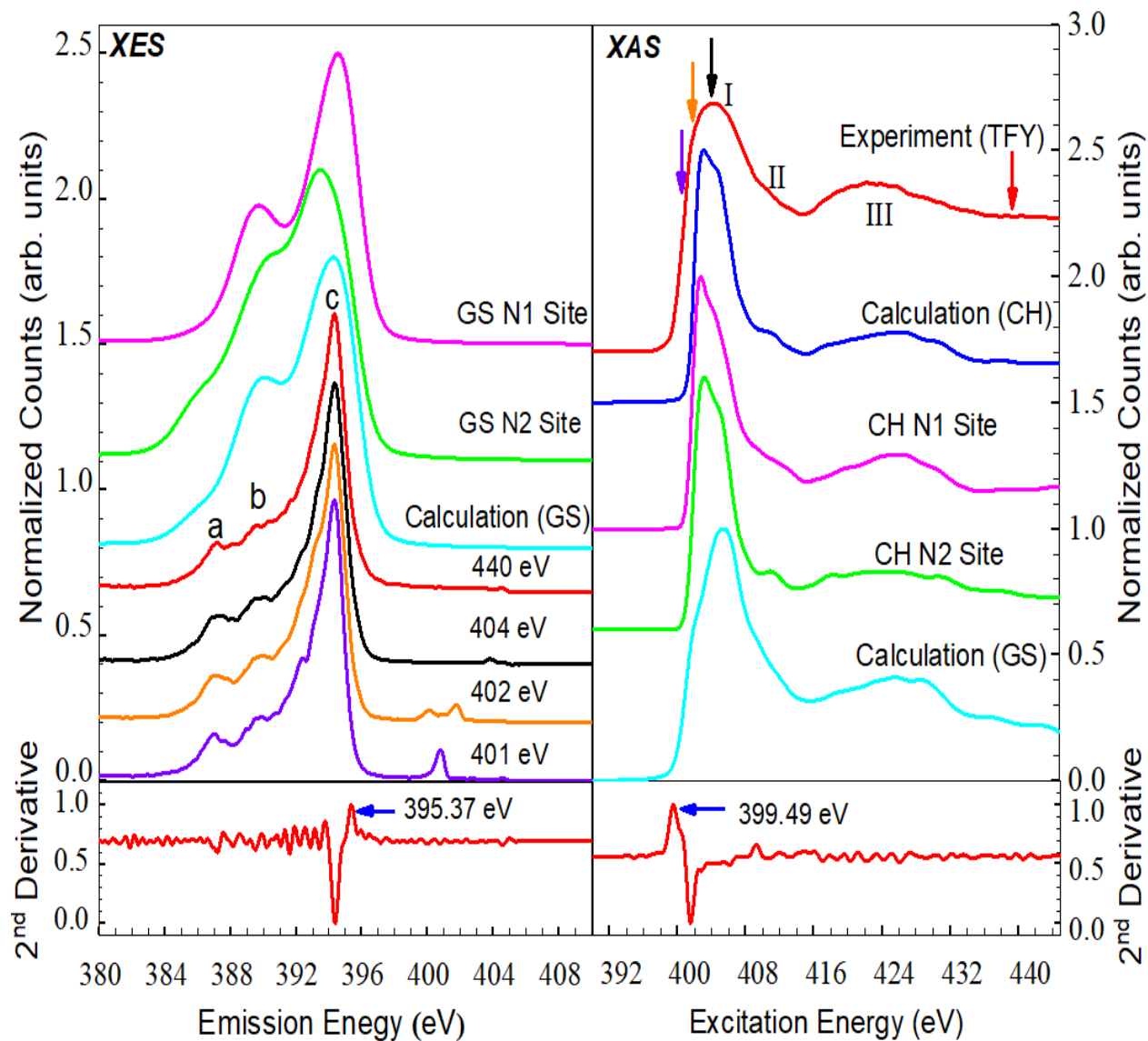
Figure 5.2. Comparison of experimental XES (left) and XAS (right) spectra with calculated spectra of Zn_2PN_3. The lower two panels show the second derivative applied to the experimental XES and XAS spectra with the corresponding maxima indicated by the blue arrows determining the valence band and conduction band edges.

Both the resonant and non-resonant XES spectra are shown in the top left panel in Figure 5.2. Although Zn_2PN_3 has two crystallographically independent nitrogen sites, the calculated pDOS for each site is almost identical throughout the conduction band. For that reason, it was not possible to excite one site predominantly and both sites are leading to indistinguishable emission spectra. The excitation energies for the RXES spectra were 401, 402, and 404 eV while the NXES spectrum was collected at 440 eV. The exact positions for these excitation energies are indicated by blue, orange, black, and red colored downward arrows on the measured XAS spectrum (top right panel - red) in Figure 5.2. Although the excitation energy is increased from 401 to 404 eV, there is no noticeable difference between them, only the elastic peaks are shifted. But the intensity of two small peaks before the main peak decreases with an increase in excitation energy from 404 to 440 eV. There are three main features labeled as a to c in the NXES spectrum (red) at 440 eV. The individual atomic contribution to the features a to c are explained with the help of two calculated spectra (magenta and green) of the non-equivalent N sites. Feature a stems from the 2p states contribution of the N2 site while feature b is contributed by 2p states of the N1 site. Feature b is more prominent in the ground state calculation but almost vanishes in the measured emission spectrum. This could be because of the 3d state contribution of Zn in calculated emission spectrum. The contributions on the main peak referred as feature c stem from 2p states of N1 site.

5.1.4 Band Gap Determination of Zn_2PN_3

Now the experimental band gap of Zn_2PN_3 is determined using the previously discussed second derivative approach. The second derivative is applied to the non-resonant XES (440 eV) and XAS spectrum displayed in the bottom two windows of Figure 5.2. A separation of 4.1 ± 0.2 eV between the VB and CB onsets is measured, resulting an overall band gap of 4.2 ± 0.2 eV with considering

the 0.1 eV shift in the core hole. The band gap of Zn_2PN_3 determined using PBE-GGA is 2.6 eV and as expected much lower than the experimental value. For a more appropriate band gap, the mBj calculation is also performed, which yields a band gap of 3.9 eV. The band gap of Zn_2PN_3 available in the literature (3.7 eV) [8] using diffuse reflectance spectroscopy which is close to the measured and mBj-calculated band gap. The data in Figure 5.2 do not allow to unambiguously decide whether the gap is direct or indirect. A summary of the band gaps of the two materials studied herein this section is shown in Table 5.1.

Table 5.1. Measured, calculated and previously reported band gaps for M_2PN_3 (M=Mg, Zn). The experimental band gaps are denoted by E_{exp}, calculated band gaps are denoted by $E_{PBE-GGA}$ and E_{mBj}.

Compound	E_{exp} [eV]	$E_{PBE-GGA}$ [eV]	E_{mBJ} [eV]	Literature [8] [eV]
Mg_2PN_3	5.3 ± 0.2	3.7	5.4	5.0
Zn_2PN_3	4.2 ± 0.2	2.6	3.9	3.7

5.1.4 Band Structure and Density of States of M_2PN_3 (M=Mg, Zn)

In this section, the mBJ calculated band gap and the PBE-GGA calculated density of states of the Mg_2PN_3 and the Zn_2PN_3 are explained in order to deliver a more detailed picture.

The calculated band structure and the density of states of Mg_2PN_3 are depicted in Figure 5.3 (a) and (b), respectively. The band structure of Mg_2PN_3 predicts an indirect band gap, which is also determined experimentally in the previous section. The k-path used in our study is derived using reference [72]. The valence band maximum lies somewhere in between the Γ and the Z point of

the Brillouin zone while the conduction band minimum is located at the Γ point resulting an indirect band gap of 5.4 eV. The energy scale is set with respect to the Fermi energy, E_F (0 eV). As the Fermi level lies in the valence band, it can be predicted that the conduction in Mg_2PN_3 would be due to the p-type charge carriers [73].

The agreement between the measured and calculated XAS and XES spectra of Mg_2PN_3 offers experimental support for the calculated density of states, which is discussed in more detail using Figure 5.3 (b). The calculated density of states of two non-equivalent N sites and the other atoms coordinating with them are shown in Figure 5.3 (b). The density of states in the valence band of Mg_2PN_3 can be divided into two sub bands: (i) the lower valence band (-10 eV to -7.5 eV) and (ii) the upper valence band (-7 eV to 0 eV). The lower valence band has a large contribution from the N2 2p states while N1 2p states contribute throughout the upper valence band. The contribution of the coordinating atoms (Mg and P) are almost negligible in the entire valence band. As it is seen in Figure 5.3 (a) and (b), the conduction band contains relatively few states from 5.5 to 7 eV. The N1, N2, P, and Mg p character dominate the conduction band from 7 to 20 eV. After this energy, the N1 and N2 p states contribution starts to decrease, and the Mg d states become more prominent. The d states contribution of P is negligible in the upper conduction band.

Like Mg_2PN_3, the calculated band structure and density of states of Zn_2PN_3 are shown in Figure 5.4 (a) and (b). The k-path used for Zn_2PN_3 is essentially the same as the Mg_2PN_3. The work in reference [8] used a different k-path than this study pointing the maximum and minimum energy value at the same Γ point, concluding that Zn_2PN_3 is a direct band gap material. But the conduction band minimum and the valence band maximum are found to be at Γ as well as Δ, respectively. As the two points are not at the same crystal momentum, one would conclude that Zn_2PN_3 has an indirect band gap.
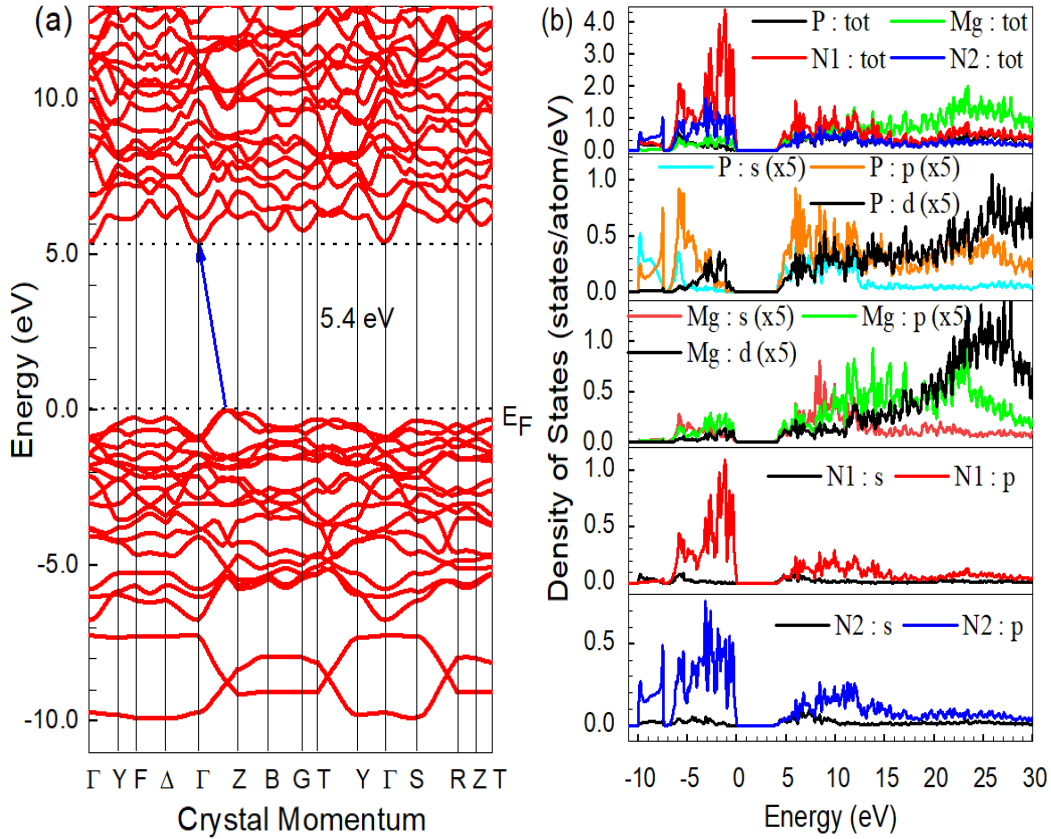
Figure 5.3. Calculated band structure and partial density of states (pDOS) of Mg_2PN_3 using the mBJ exchange potential. (a) Calculated band structure: The indirect transition between the conduction band minimum (at Γ point) and the valence band maximum (in between the Γ and Z point) is shown by a blue arrow. The edge of the valence band is set to E_F (0 eV). (b) The partial density of electronic states are shown for the respective elements N1, N2, P, and Mg along with the symmetry of the wavefunction. The pDOS value of each character for Mg and P are increased by a factor of 5.

Figure 5.4 (b) shows the total and partial density of states of Zn_2PN_3 which will be discussed now. To analyze the density of states, the valence band is divided into three regions: (i) the lower valence
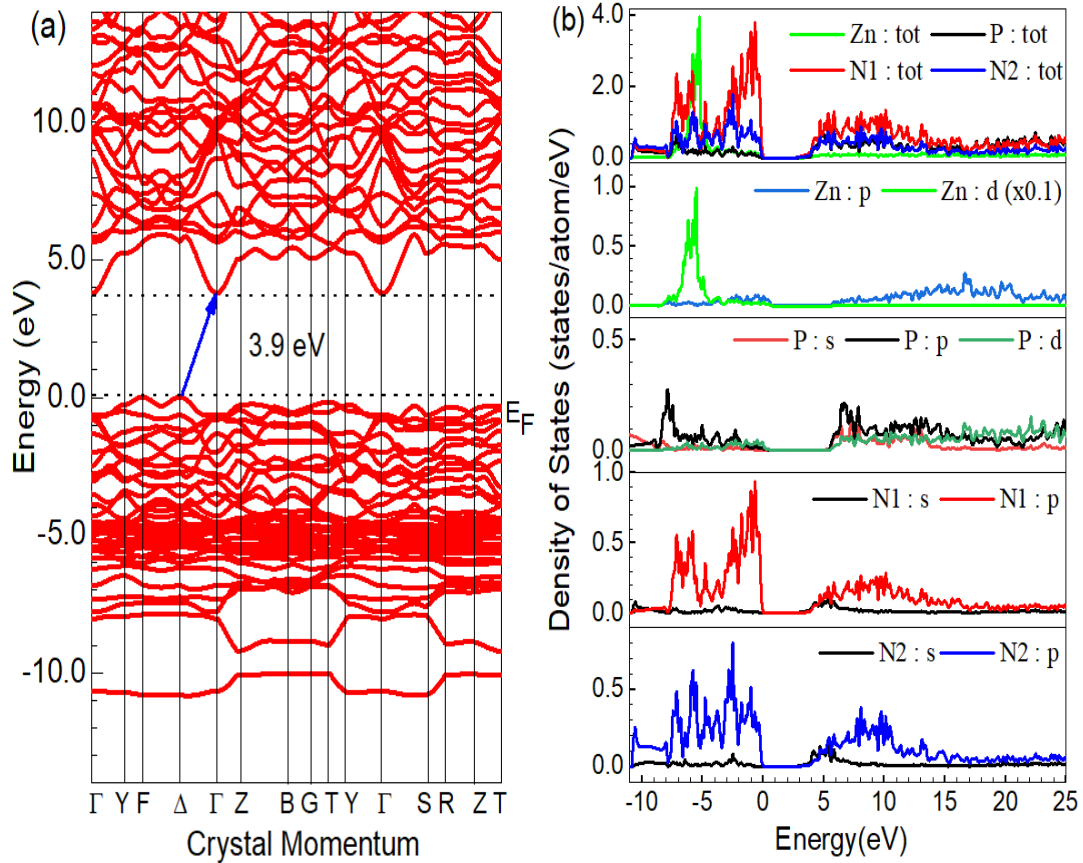
Figure 5.4. (a) The band structure and (b) calculated partial density of states (DOS) of Zn_2PN_3.

band (-11 eV to -8 eV), (ii) the middle valence band (-8 eV to -4 eV), and (iii) the upper valence band (-4 eV to 0 eV). The lower part of the valence band is dominated by the contribution of 2p states of N2 site. The hybridization of the highly localized Zn 3d states with the N1 2p states is seen in the middle part of the valence band. At the upper valence band near the Fermi level (0 eV), the contributions stem from 2p states of the N1 site. On the other hand, the total density of states in the conduction band is almost evenly distributed between the p states of phosphorus (atom P) and the two non-equivalent N sites while the contribution of Zn is almost zero.

P, and N both have valence electron configuration of s^2p^3, while Mg has s^2, and Zn has $d^{10}s^2$. For

both crystals, there are four-unit formula per unit cell [8]. Hence the total valance electrons in a unit cell is 96 for Mg_2PN_3, and 156 for Zn_2PN_3. Including spin degeneracy, it is expected that the total number of energy bands within valence band to be 48 for Mg_2PN_3, and 78 for Zn_2PN_3. Contribution of N s electrons for both materials is well below the Fermi level between -18.8 eV to -16.2 eV and are not shown in Figure 5.3 (a) and Figure 5.4 (a). Figure 5.3 (a) shows 18 bands for Mg_2PN_3 and Figure 5.4 (a) shows 51 bands for Zn_2PN_3, which is fewer than expected due to the energy degeneracy of the bands and as stated above because some bands lie well below the Fermi level. N p-states contribute throughout the VB near the Fermi level (0 eV to -10 eV) but there is weak admixture of N s states with N p states in the lower VB (-7 eV to 0 eV).

5.2 Non-metallic Nitridophosphate, BP_3N_6

5.2.1 N K-edge Spectra of BP_3N_6

Unlike the metallic nitridophosphates, Mg_2PN_3 and Zn_2PN_3, this BP_3N_6 has a complex crystal structure in terms of number of atoms per unit cell. While the Mg_2PN_3 and Zn_2PN_3 has only two non-equivalent nitrogen sites, BP_3N_6 has six non-equivalent nitrogen sites which make it more complex to calculate the X-ray absorption and X-ray emission spectra. The N K-edge spectra of BP_3N_6 were collected instead of B since N XES measurements offer a very sharp peak which is ideal for choosing the valence band onset while applying the second derivative. However, the choice of N spectra in the case of BP_3N_6 complicates the problem of displaying the calculated six non-equivalent N sites. For that reason, the importance of non-equivalent N sites is discussed using the density of states calculation instead of XAS and XES spectra of these non-equivalent sites.
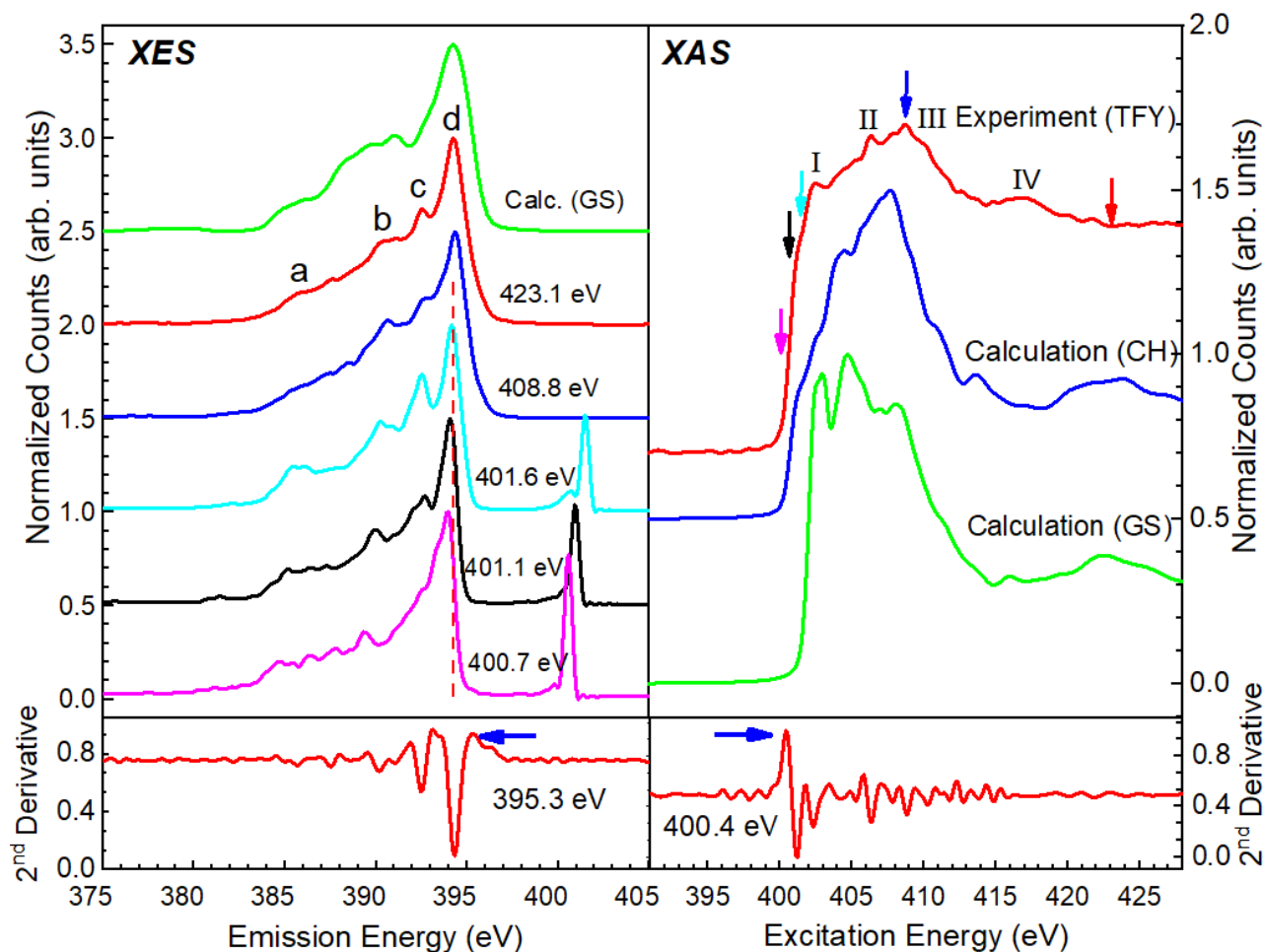
Figure 5.5. Measured and simulated N 1s XAS (top right Panel) and N K_α XES (top left panel) spectra of BP_3N_6. Valence band (bottom left) and conduction band (bottom right) onsets are determined applying the second derivative on the experimental XES and XAS spectra.

The N 1s XAS spectra of BP_3N_6 are displayed on the top right portion of Figure 5.5. The absorption spectra of each non-equivalent N site are simulated separately for both core hole and the ground state and then added together to get the entire solid-state absorption spectrum.

The core hole and the ground state spectra of BP_3N_6 are displayed in blue and green color respectively on the top right panel of Figure 5.5 which are linear combination of six non-equivalent N sites.

The experimental absorption spectrum is collected in TFY mode shown in red color. As described in the experimental section, the XAS spectra have been normalized to the incident photon flux. The general behaviour and four key features denoted as I through IV on the experimental TFY spectrum are reproduced in the calculated core hole spectrum. The spectral feature I at 402.6 eV arises from the p states contribution of P1 atom. Feature II and III at 406.4 eV and 408.9 eV respectively, stem from the mixture of s states of N2 and p states of B. Finally, the feature IV at 417.3 eV results from the p states of B and the d states of P1.

The top left panel of Figure 5.5 displays the measured and calculated XES spectra. Six crystallographic distinct N sites in the crystal structure of BP_3N_6 made it difficult to excite a particular site predominantly. Despite having six non-equivalent site of N, the individual emission spectra are almost indistinguishable from each other. The resonant emission spectra of BP_3N_6 were measured at 400.7 eV, 401.1 eV, 401.6 eV, and 408.8 eV all of which show the similar spectral feature. The non-resonant emission spectrum excited at 423.1 eV agrees well with the calculated ground state spectrum. Feature a in the experimental spectrum originates from the 2p states of N6 atom while the features b and c stem from 2p states of N1 and N2 atom. Most of the contribution on the main peak b at 398.3 eV are derived from the 2p states contribution of N5 and N6.

As discussed earlier, the RXES spectra excited along the conduction band edge can be used to determine whether the band gap is direct or indirect. Here, the RXES spectra excited at 400.7 eV, 401.1 eV and 401.6 eV show that the highest emission energy occurs at higher excitation energy.

This is shown drawing a vertically dotted red line in the top left panel of Figure 5.5. Therefore, the band gap of BP_3N_6 is indirect.

5.2.2 Band Gap Determination and Band Structure of BP_3N_6

The experimental band gap of BP_3N_6 is now determined using the second derivative approach discussed above for the other two samples, Mg_2PN_3 and Zn_2PN_3. Applying the second derivative on the XES and XAS experimental spectra, a gap between VB and CB of 5.1 eV is determined. A 0.2 eV shift in the core hole resulting the final band gap of 5.3 ± 0.2 eV. The band gap of BP_3N_6 calculated using PBE-GGA is 4.5 eV which is lower than the experimentally determined band gap. More suitable band gap of 5.8 eV is determined performing the mBj calculation. Until now, there is no reported band gap value of BP_3N_6 available in the literature which does not allow to compare the results. A summary of the measured and calculated band gap of BP_3N_6 is given in Table 5.2.

Table 5.2. Measured and calculated band gap of BP_3N_6. The experimental band gaps are denoted by E_{exp}, calculated band gaps are denoted by $E_{PBE-GGA}$ and E_{mBj}.

Compound	E_{exp} [eV]	$E_{PBE-GGA}$ [eV]	E_{mBJ} [eV]	Literature [eV]
BP_3N_6	5.3 ± 0.2	4.5	5.8	N/A

After having discussed the band gap, now the electronic band structure of BP_3N_6 is considered. The mBJ calculated electronic structure is shown in Figure 5.6 (a). The conduction band has a minimum at the point between Σ and Δ while the valence band maximum is found to be at the Σ point. The calculated band bap of BP_3N_6 is predicted to be indirect which agrees with the experimental results. The bands are evenly distributed throughout the conduction band. On the
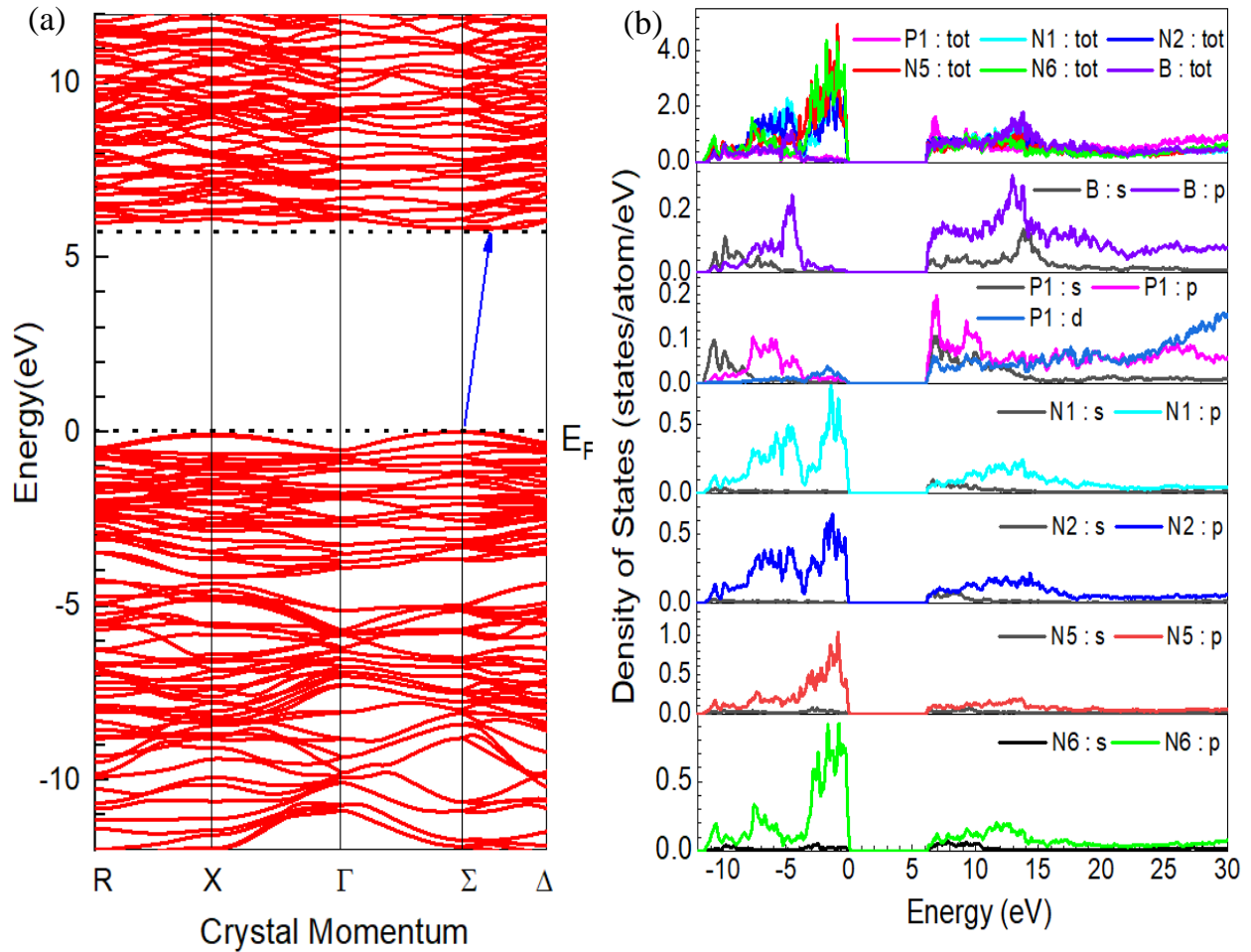
Figure 5.6. (a) The band structure and (b) calculated density of states of BP_3N_6.

other hand, the bands in the vicinity of the valence band maximum are dense enough leading to a significant peak in the density of states.

5.2.3 Density of States of BP_3N_6

Like the XAS calculation, the density of the states can be calculated separately for each site inside the crystal. Such calculations of the density of states offer a straightforward reflection of the

relative energy positions of the orbitals without the core hole effect. Since the XAS calculations are based on the perturbed DOS results, the close agreement that was found between the experimental and theoretical spectra suggests that the unperturbed DOS calculations provide an accurate portrayal of the ground state electronic structure of the crystal [74].

The PBE-GGA calculated density of states of BP_3N_6 is shown in Figure 5.6 (b). The entire valence band is comprised of three regions indicated in descending energy with VB_1, VB_2, and VB_3. Near the fermi energy (0 eV), the valence band shows a very sharp edge. VB_1 in the energy range of 0 eV to -4 eV, is dominated by p states of N5, N6, and N2. VB_2 from -4 eV to -8 eV has a contribution from p states of N1 and N2 while most of the contribution in region VB_3 from -8 eV to -11.5 eV is coming from the p states of the N6 site. The two peaks in the conduction band at 6.9 eV and 9.5 eV are mostly contributed from the p states of P1. Between the two peaks, N1, N6 and B contribute evenly. After energy 9.5 eV, the contribution of p states of B starts to increase while other co-ordinating atoms contribution begins to decrease.

Chapter 6

Conclusion

6.1 Summary of Results

Soft X-ray spectroscopy using the radiation from a synchrotron source is a powerful technique which provides insight into the electronic structure of a material that would otherwise be inaccessible. This thesis represents significant new outcomes in the investigation of electronic structure and band gap of newly synthesized nitridophosphate materials by means of X-ray absorption and X-ray emission spectroscopy techniques.

The electronic structure and the band gap of ammonothermally synthesized M_2PN_3(M=Mg, Zn) and BP_3N_6 have been probed experimentally and theoretically using soft X-ray spectroscopy measurements and density functional theory calculations, respectively. Excellent agreement is observed between the measured and calculated N 1s XAS and N K-edge XES spectra which supports crystal structures employed for the calculations for M_2PN_3(M=Mg, Zn) and BP_3N_6 as well as the approach in a single electron picture. The measured band gap of 5.3 ± 0.2 eV (Mg_2PN_3), 4.2 ± 0.2 eV (Zn_2PN_3), and 5.3 ± 0.2 eV (BP_3N_6) is in good agreement with mBJ-calculated band gap of 5.4 eV for Mg_2PN_3, 3.9 eV for Zn_2PN_3 and 5.8 eV for BP_3N_6. The results obtained in this thesis is also in qualitative agreement with previously published UV-Vis measurements of the sample, Mg_2PN_3 and Zn_2PN_3, but no experimental and theoretical data has yet been published for BP_3N_6. All the three materials have been reported to have an indirect wide band gap. The findings

obtained of the materials studied herein, provide a means for enhanced understanding in designing

future efficient (opto)electronic devices.

References

[1]   N. Senabulya, "Structural Characterization Studies on Semiconducting $ZnSnN_2$ Films Using Synchrotron X-ray Diffraction", Ph.D. Thesis, University of Michigan, 2017.

[2]   P. Jackson, H. Dimitrios, L. Erwin, P. Stefan, W. Roland, M. Richard, W. Wiltraud, and P. Michael, "New World Record Efficiency for Cu(In, Ga)Se_2 Thin-Film Solar Cells Beyond 20%", *Progress in Photovoltaics: Research and Applications* **19**, 894-897, 2011.

[3]   A. Romeo, M. Terheggen, D. Abou-Ras, D. L. Bätzner, F. J. Haug, M. Kälin, D. Rudmann, and A. N. Titwari, "Development of Thin-Film Cu(In,Ga)Se_2 and CdTe Solar Cells", *Progress in Photovoltaics: Research and Applications* **12**, 93-111, 2004.

[4]   S. D. Kloß and W. Schnick, "Nitridophosphates - A Success Story of Nitride Synthesis", *Angewandte Chemie International Edition* **58**, 7933-7944, 2019.

[5]   T. M. Tolhurst, C. Braun, T. D. Boyko, W. Schnick, and A. Moewes, "Experiment-Driven Modeling of Crystalline Phosphorus Nitride P_3N_5 : Wide-Ranging Implications from a Unique Structure", *Chemistry - A European Journal* **22**, 10475–10483, 2016.

[6]   W. Schnick, "Solid-State Chemistry with Nonmetal Nitrides", *Angewandte Chemie International Edition in English* **32**, 806-818, 1993.

[7]   S. J. Sedlmaier, M. Eberspächer, and W. Schnick, "High-pressure synthesis, crystal structure, and characterization of Zn_2PN_3 - A New Catena-Polynitridophosphate", *Zeitschrift für anorganische und allgemeine Chemie* **637**, 362–367, 2011.

[8]   M. Mallmann, C. Maak, R. Niklaus, and W. Schnick, "Ammonothermal Synthesis, Optical Properties, and DFT Calculations of Mg_2PN_3 and Zn_2PN_3", *Chemistry - A European Journal* **24**, 13963–13970, 2018.

[9]   V. C. Schultz, and W. Schnick, "Mg$_2$PN$_3$ and Ca$_2$PN$_3$ Phosphorus (V) Nitrides with One-Dimensional Infinite Chains of Corner-Sharing PN$_4$ Tetrahedra", *Journal of Inorganic and General Chemistry* **623,** 69-74, 1997.

[10]   S. Vogel, A. T. Buda, and W. Schnick, "United in Nitride: The Highly Condensed Boron Phosphorus Nitride BP$_3$N$_6$", *Angewandte Chemie International Edition*, **57**, 13202-13205, 2018.

[11]   W. Schnick, and V. Schultz-Coulon, "Ca$_2$PN$_3$: A New Phosphorus (V) Nitride with One-Dimensional Infinite Chains of Corner-Sharing PN$_4$ Tetrahedra", *Angewandte Chemie International Edition in English* **32**, 280-281,1993.

[12]   L. F. Riley, "Silicon Nitride and Related Materials", *Journal of the American Ceramic Society* **83,** 245-265, 2000.

[13]   J. Kopac, and K. Peter, "High-Performance Grinding - A Review", *Journal of Materials Processing Technology* **175,** 278-284, 2006.

[14]   J. Wen, J. Xie, X. Chen, and X. Li, "A Review on g-C$_3$N$_4$ Based Photocatalysts", *Applied surface science* **391**, 72-123, 2017.

[15]   L. C. Tien, and C. H. Ho, "Synthesis, Optical Characterization, and Environmental Applications of β-Ga$_2$O$_3$ Nanowires", *Gallium Oxide* (Amsterdam, New York: Elsevier) 67-90, 2019.

[16]   M. Caglar, S. Ilican, and Y. Caglar, "Structural, Morphological, and Optical Properties of CuAlS$_2$ Films Deposited by Spray Pyrolysis Method", *Optics Communications*, **281**, 1615-1624, 2008.

[17]   C. H. Ho, "Thermoreflectance Characterization of Band-Edge Excitonic Transitions in CuAlS$_2$ Ultraviolet Solar-Cell Material", *Applied Physics Letters* **96**, 061902, 2010.

[18] Y. Zou, Y. Zhang, Y. Hu, and H. Gu, "Ultraviolet Detectors Based on Wide Bandgap Semiconductor Nanowire: A Review", *Sensors* **18**, 2072, 2018.

[19] M. Delor, P. A. Scattergood, I. V. Sazanovich, A. W. Parker, G. M. Greetham, A. J. H. M. Meijer, M. Towrie, and J. A. Weinstein, "Toward Control of Electron Transfer in Donor-Acceptor Molecules by Bond-Specific Infrared Excitation", *Science* **346**, 1492–1495, 2014.

[20] H. Chen, K. Liu, L. Hu, A. A. Al-Ghamdi, and X. Fang, "New Concept Ultraviolet Photodetectors", *Materials Today* **18**, 493-502, 2015.

[21] D. Wu, Q. Hu, Z. Yan, W. Chen, C. Yan, X. Huang, J. Zhang, P. Yang, H. Deng, J. Wang, and X. Deng, "Structural Basis of Ultraviolet-B Perception by UVR8", *Nature* **484**, 214, 2012.

[22] S. Premi, S. Wallisch, C. M. Mano, A. B. Weiner, A. Bacchiocchi, K. Wakamatsu, E. J. Bechara, R. Halaban, T. Douki, and D. E. Brash, "Chemiexcitation of Melanin Derivatives Induces DNA Photoproducts Long After UV Exposure", *Science* **347**, 842-847, 2015.

[23] Y. Hinuma, T. Hatakeyama, Y. Kumagai, L. A. Burton, H. Sato, Y. Muraba, S. Iimura, H. Hiramatsu, I. Tanaka, H. Hosono, and F. Oba, "Discovery of Earth-Abundant Nitride Semiconductors by Computational Screening and High-Pressure Synthesis", *Nature Communications* **7**, 11962, 2016.

[24] T. de Boer, T. D. Boyko, C. Braun, W. Schnick, and A. Moewes, "Band Gap and Electronic Structure of $MgSiN_2$ Determined Using Soft X-ray Spectroscopy and Density Functional Theory", *Physical Status Solidi - Rapid Research Letters* **9**, 250–254, 2015.

[25] E. Constable, "Comprehensive Coordination Chemistry II: from Biology to Nanotechnology", *Elsevier*, 2003.

[26] F. R. Elder, A. M. Gurewitsch, R. V. Langmuir, and H. C. pollock, "Radiation from Electrons in a Synchrotron", *Physical Review* **71,** 829,1947.

[27] P. J. de Pablo, F. Moreno-Herrero, J. Colchero, J. G. Herrero, P. Herrero, A. M. Baro, P. Ordejon, J. M. Soler, and E. Artacho, "Absence of DC-Conductivity in λ-DNA", *Physical Review Letters* **85**, 4992, 2000.

[28] A. J. Storm, J. van Noort, S. de Vries, and C. Dekker, "Insulating Behavior for DNA Molecules Between Nanoelectrodes at the 100 nm Length Scale", *Applied Physics Letters* **79**, 3881-3883, 2001.

[29] R. G. Wilks, "X-ray Spectroscopy of Organic Materials", Ph.D. Thesis, University of Saskatchewan, 2009.

[30] P. Willmott, "An Introduction to Synchrotron Radiation: Techniques and Applications", *Wiley*, Hoboken, NJ, USA, 2011.

[31] M. F. L'Annunziata, "Radioactivity: Introduction and History, from the Quantum to Quarks", *Elsevier,* 2016.

[32] https://www.lightsource.ca/inside_the_synchrotron (June 7, 2020).

[33] K. Baptiste, P. Casey, S. Kwiatkowski, and C. Timossi, "Results of the ALS Booster Ring RF System Upgrade for Top-off Mode of Operation" *IEEE Particle Accelerator Conference (PAC)*, 2307-2309, 2007.

[34] J. A. Clarke, "The Science and Technology of Undulators and Wigglers", *Oxford University Press on Demand*, **4,** 2004.

[35] D. Muir, "A Soft X-Ray Emission Endstation for the Canadian Light Source", Ph.D. Thesis, University of Saskatchewan, 2013.

[36] https://commons.wikimedia.org/wiki/File:Undulator.png (June 7, 2020)

[37] D. Attwood, and A. Sakdinawat, "X-rays and Extreme Ultraviolet Radiation: Principles and Applications", *Cambridge University Press*, 2017.

[38] E. McDermott, "Study of Solid State Photocatalysts and Other Energy Materials using Synchrotron Radiation" MSc Thesis, University of Saskatchewan, 2012.

[39] https://sites.google.com/a/lbl.gov/beamline-8-0-1-reference/ (June 7, 2020).

[40] https://www.wikiwand.com/en/Auger_electron_spectroscopy (11 March, 2020).

[41] J. Stöhr, "NEXAFS Spectroscopy", *Springer Science & Business Media* **25,** 2013.

[42] W. Crookes, "V. The Bakerian Lecture - On the Illumination of Lines of Molecular Pressure, and the Trajectory of Molecules", *Philosophical Transactions of the Royal Society of London* **170**, 135-164, 1879.

[43] W. Kossel, "To Build the X-ray Spectra", *Journal of Physics* **1**, 119-134, 1920.

[44] https://www.ucalgary.ca/live-uc-ucalgary-site/sites/default/files/teams/269/xas.pdf (March 22, 2020).

[45] G. D. Mahan, "Final-state Potential in X-ray Spectra", *Physical Review B*, **21**, 1421, 1980.

[46] J. A. McLeod, "EXAFS Study of Amorphous Selenium", Ph.D. Thesis, University of Saskatchewan, 2010.

[47] R. Marchand, and Y. Laurent, "Demonstration of PN_4 Tetrahedra in Wurtzite Nitride Mg_2PN_3", *Materials Research Bulletin* 17, 399-403, 1982.

[48] D. Ehrentraut, E. Meissner, and M. Bockowski, "Technology of Gallium Nitride Crystal Growth", *Springer Science & Business Media* **133,** 2010.

[49] F. Kawamura, N. Yamada, M. Imai, and T. Taniguchi, "Synthesis of $ZnSnN_2$ Crystals via a High-pressure Metathesis Reaction", *Crystal Research and Technology* **51**, 220-224, 2016.

[50] M. Mallmann, J. Häusler, N. Cordes, and W. Schnick, "Ammonothermal Synthesis of Alkali-Alkaline Earth Metal and Alkali-Rare Earth Metal Carbodiimides: $K_{5-x}M_x$ $(CN_2)_{2+x}(HCN_2)_{1-x}$(M= Sr, Eu) and $Na_{4.32}Sr_{0.68}(CN_2)_{2.68}(HCN_2)_{0.32}$" *Zeitschrift für Anorganische und Allgemeine Chemie* **643**, 1956-1961, 2017.

[51] J. Hausler, S. Schimmel, P. Wellmann, and W. Schnick, "Ammonothermal Synthesis of Earth-Abundant Nitride Semiconductors $ZnSiN_2$ and $ZnGeN_2$ and Dissolution Monitoring by In Situ X-ray Imaging", *Chemistry-A European Journal* **23**, 12275-12282, 2017.

[52] J. Häusler, and W. Schnick, "Ammonothermal Synthesis of Nitrides: Recent Developments and Future Perspectives", *Chemistry-A European Journal* **24,** 11864-11879, 2018.

[53] N. Cordes, and W. Schnick, "Ammonothermal Synthesis of Crystalline Oxonitride Perovskites $LnTaON_2$(Ln= La, Ce, Pr, Nd, Sm, Gd)", *Chemistry-A European Journal* **23,** 11410-11415, 2017.

[54] T. M. Richter, and R. Niewa, "Chemistry of Ammonothermal Synthesis", *Inorganics* **2**, 29-78, 2014.

[55] F. L. Riley, "Silicon Nitride and Related Materials", *Journal of the American Ceramic Society* **83,** 245-265, 2000.

[56] J. Kopac, and P. Krajnik, "High-performance Grinding-A Review", *Journal of Materials Processing Technology* **175,** 278-284, 2006.

[57] J. Guo, "Synchrotron radiation, soft-X-ray spectroscopy and nanomaterials", *International Journal of Nanotechnology* **1**, 193-225, 2004.

[58] R. Clarke, "Incoherent Sources: Synchrotrons", in *Encyclopedia of Modern Optics*, Elsevier 217-224, 2005.

[59] M. Boots, D. Muir, and A. Moewes, "Optimizing and Characterizing Grating Efficiency for a Soft X-Ray Emission Spectrometer", *Journal of Synchrotron Radiation* **20**, 272-285, 2013.

[60] J. J. Jia, T. A. Callcott, J. Yurkas, A. W. Ellis, F. J. Himpsel, M. G. Samant, J. Stöhr, D. L. Ederer, J. A. Carlisle, E. A. Hudson, and L. J. Terminello, "First Experimental Results from IBM/TENN/TULANE/LLNL/LBL Undulator Beamline at the Advanced Light Source", *Review of Scientific Instruments* **66**, 1394-1397, 1995.

[61] T. M. Tolhurst, T. D. Boyko, P. Pust, N. W. Johnson, W. Schnick, and A. Moewes, "Investigations of the Electronic Structure and Bandgap of the Next-Generation LED-Phosphor Sr[LiAl$_3$N$_4$]:Eu^{2+}-Experiment and Calculations ", *Advanced Optical Materials* **3**, 546–550, 2015.

[62] J. A. McLeod, R. G. Wilks, N. A. Skorikov, L. D. Finkelstein, M. Abu-Samak, E. Z. Kurmaev, A. Moewes, "Band Gaps and Electronic Structure of Alkaline-Earth and Post-Transition-Metal Oxides", *Physical Review B* **81**, 1–9, 2010.

[63] K. Schwarz, P. Blaha, and G. K. H. Madsen, "Electronic Structure Calculations of Solids Using the WIEN2k Package for Material Sciences", *Computer Physics Communication* **147**, 71–76, 2002.

[64] W. Kohn, and L. J. Sham, "Self-Consistent Equations Including Exchange And Correlation Effects", *Physical Review* **140**, A1133, 1965.

[65] J. A. Mcleod, R. J. Green, E. Z. Kurmaev, N. Kumada, A. A. Belik, and A. Moewes, "Band-Gap Engineering in Tio$_2$-Based Ternary Oxides", *Physical Review B* **85**, 1–8, 2012.

[66] K. Schwarz, A. Neckel, and J. Nordgren, "On the X-ray Emission Spectra from FeAl", *Journal of Physics F: Metal Physics* **9**, 2509–2521, 1979.

[67] R. J. Green, T. Z. Regier, B. Leedahl, J. A. McLeod, X. H. Xu, G. S. Chang, E. Z. Kurmaev, and A. Moewes, "Adjacent Fe-Vacancy Interactions as the Origin of Room Temperature Ferromagnetism in (In$_{1-x}$ Fe$_x$)$_2$O$_3$", *Physical Review Letters* **115**, 167401-167406, 2015.

[68] S. Eisebitt, and W. Eberhardt, "Band Structure Information and Resonant Inelastic Soft X-Ray in Broad Band Solids*", Journal of Electron Spectroscopy and Related Phenomena* **110**, 335-358, 2000.

[69] J. P. Perdew, K. Burke, and M. Ernzerhof, "Generalized Gradient Approximation Made Simple", *Physical Review Letters* **77**, 3865-3868, 1996.

[70] A. D. Becke, and E. R. Johnson, "A Simple Effective Potential for Exchange", *Journal of Chemical Physics* **124,** 221101-221104, 2006.

[71] F. Tran, and P. Blaha, "Accurate Band Gaps of Semiconductors and Insulators with a Semilocal Exchange-Correlation Potential", *Physical Review Letters* **102**, 226401-226404, 2009.

[72] Y. Hinuma, G. Pizzi, Y. Kumagai, F. Oba, and I. Tanaka, "Band Structure Diagram Paths Based on Crystallography", *Computational Material Science* **128**, 140-184, 2017.

[73] A. KoleŻyński, and W. Szczypka, "First-Principles Study of the Electronic Structure and Bonding Properties of X_8C_{46} and $X_8B_6C_{40}$ (X: Li, Na, Mg, Ca) Carbon Clathrates", *Journal of Electronic Materials* **45**, 1336-1345, 2016.

[74] R. G. Wilks, "Experimental and Theoretical Investigation of the Electronic Structures of Ferrocene-Peptide Conjugates", MSc Thesis, University of Saskatchewan, 2005.